Invited Research Article

The discovery of the southernmost ultra-high-resolution Holocene paleoclimate sedimentary record in Antarctica

Francesca Battaglia [a,b,*], Laura De Santis [a], Luca Baradello [a], Ester Colizza [c], Michele Rebesco [a], Vedrana Kovacevic [a], Laura Ursella [a], Manuel Bensi [a], Daniela Accettella [a], Danilo Morelli [d], Nicola Corradi [d], Pierpaolo Falco [e], Naomi Krauzig [e], Florence Colleoni [a], Emiliano Gordini [a], Andrea Caburlotto [a], Leonardo Langone [b], Furio Finocchiaro [c]

[a] National Institute of Oceanography and Applied Geophysics – OGS, Sgonico 34010, Italy
[b] Institute of Polar Sciences - National Council of Research (CNR-ISP), Via P. Gobetti 101, 40129 Bologna, Italy
[c] University di Trieste, Department of Mathematics, Informatics and Geosciences, Via Edoardo Weiss, 2, 34128 Trieste, TS, Italy
[d] University of Genoa, Department of Earth, Environmental and Life Sciences – DISTAV, Corso Europa, 26, 16132 Genoa, GE, Italy
[e] Marche Polytechnic University, Via Brecce Bianche, 60121 Ancona, AN, Italy

ARTICLE INFO

ABSTRACT

The response of the Antarctic ice sheet to climate warming is the main source of uncertainty regarding future global sea level rise, since little is known about its present and past dynamics. The last deglaciation is the most recent interval of large-scale climate warming, during which the Northern and Southern Hemisphere ice sheets retreated, and sea level rose globally, although at a non-uniform rate. Geologic records from the polar regions are fundamental in determining the factors that caused the major changes in ice sheets during the last deglacial under different boundary conditions. Here, we combine morpho-bathymetric and seismic data with sediment cores and oceanographic measurements to reconstruct the processes that influenced the deposition of the southernmost, most extensive, ultrahigh-resolution record of the Holocene in Edisto Inlet fjord (Ross Sea, Antarctica). We find that post-glacial sedimentation resulted in a layered diatom mud up to 110 m thick that was locally redistributed by bottom currents over confined drifts-moats in the central part of the fjord. After the Holocene climatic optimum, the fjord was not carved by ground ice, and there continued to be internal fjord water circulation associated with Ross Sea circulation. These results support a retreat of coastal glaciers by about 11 kiloyears ago (ka) from the continental shelf of North Victoria Land.

1. Introduction

The last deglaciation is the most recent interval of large-scale climate warming, during which the Northern and Southern Hemisphere ice sheets retreated, and sea level rose at an uneven pace. The Antarctic ice sheet is the primary source of uncertainty about future sea level rise, but little is known about the chronology and mechanisms of deglaciation. Existing continental reconstructions of Antarctic ice sheet (AIS) retreat during the last deglaciations (Jouzel et al., 1995; Hodgson et al., 2014; Weber et al., 2014) show that AIS underwent significant changes after the Last Glacial Maximum (LGM, ~21 kiloyears ago, ka) (Bentley et al., 2014; Golledge et al., 2021). However, in the Ross Sea, where most of the ice sheet has advanced to the continental shelf (Anderson et al.,

2014; Bentley et al., 2014), the deglacial history is still debated. In this region, the ice sheet grounds below sea level (Hall and Denton, 1999; Hall et al., 2013) and therefore responds not only to atmospheric warming but also to ocean warming (Lowry et al., 2020). Compilations of ocean data suggest that retreat between the eastern (Bart et al., 2018) and western Ross Sea (Halberstadt et al., 2016) was not simultaneous, with periods of grounding-line stability interrupted by episodes of rapid retreat. This has generally been attributed to differences in pinning areas in the seafloor geomorphology (Anderson et al., 2019; Still et al., 2019). In the western Ross Sea, marine data suggest that the ice sheet had largely retreated by 15 ka (Prothro et al., 2020). However, the grounding line position along the coasts of Victoria Land is only partially known and has been tentatively located to about 8–4 ka offshore


(Prothro et al., 2020).

Additional marine data from this area are needed to fill this knowledge gap. The coastal fjords of North Victoria Land (NVL) are ideal environments to obtain geologic records of LGM glacial dynamics because they act as natural sediment traps, thus preserving high-resolution post-LGM archives. Indeed, sediment accumulation has been observed in Antarctic fjords and coastal bays (Griffith and Anderson, 1989; Rebesco et al., 1998; Cunningham et al., 1999; Domack and Mcclennen, 1996; Domack et al., 1999; Sjunneskog and Taylor, 2002; McMinn et al., 2001; Domack et al., 2003; Mosola and Anderson, 2006; Escutia and Brinkhuis, 2014; McGlannan et al., 2017; Ashley et al., 2021; Crosta et al., 2021), where tidewater glaciers expose and deeply incise the fjord seafloor during ice extension.

Here we report the first southernmost record of an extensive, ultra-high-resolution, Holocene sedimentary section deposited in Edisto Inlet fjord (NVL, Fig. 1) to advance knowledge of the retreat to LGM from the western Ross Sea. Data were collected during four Italian Antarctic Research Program (PNRA) campaigns aboard the research vessels Italica, OGS Explora, and Laura Bassi during favourable austral summers with little or no sea ice cover between 2002 and 2020. Following the pioneer study at the entrance of the fjord (Finocchiaro et al., 2005; Morelli et al., 2008), bathymetric and reflection seismic data combined with sediment records and oceanographic measurements demonstrate that most of the post-LGM sedimentation was influenced by the deposition of biogenic material (mainly diatom ooze) that was locally redistributed by bottom water currents. The interaction of the high sedimentation rate due to high productivity and the persistent fjord-like circulation resulted in the formation of confined drift moats and the accumulation of a sediment layer up to 110 m thick in the central inner part of the fjord. This work provides unprecedented
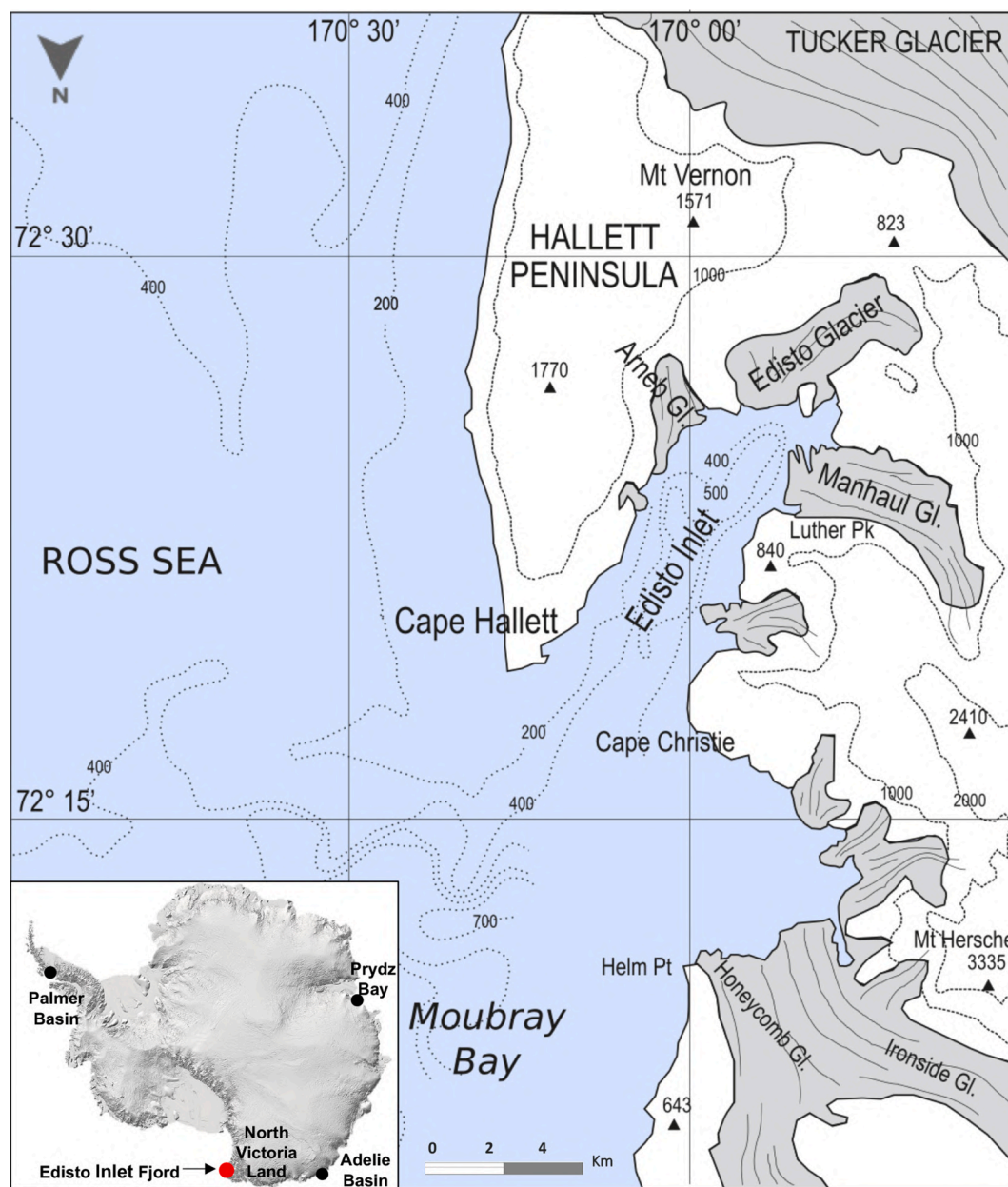
Fig. 1. Map of Edisto Inlet located between Cape Hallett and Cape Christie in the western Ross Sea (Northern Victoria Land, Antarctica). The lower left square shows the map of Antarctica with the location of Edisto Inlet (red dot), the Adelie Basin and Prydz Bay in East Antarctica and the Palmer Basin in the Antarctic Peninsula (black dots). Bathymetric data and land morphology from map SS 58–60/2 (Cape Hallett). (For interpretation of the references to colour in this figure legend, the reader is referred to the web version of this article.)

detailed seismic and morphological information on this sedimentary deposit, supported by sedimentological information. The high resolution of the acoustic data grid makes it possible to reconstruct the paleo-circulation in the fjord that led to sediment accumulation after the LGM. The results can be used to understand oceanic processes affecting the continental margin of northern Victoria Land and to constrain ice sheet retreat from the Ross Sea after the LGM.

2. Regional setting

Edisto Inlet (72°19′S 170°16′E) is a narrow and NNE-SSW elongated fjord (16 km long and 4 km wide) located between Cape Hallett and Cape Christie along the NVL coast in the western Ross Sea (Fig. 1). Its bathymetry shows a step-like, landward SW depression profile, and the fjord is separated from Moubray Bay by a sill about 400 m deep.

The fjord serves as an outlet for three ice-tongue glaciers (Fig. 2): the Manhaul Glacier (16 km long and 7 km wide), the Arneb Glacier (6 km long and 4 km wide), which flows northwest into Edisto Inlet and the Edisto Glacier (10 km long and 6 km wide). Large calving rates derived

from remote sensing indicate that Manhaul Glacier experienced a large calving event between 1989 and 1999 (Fountain, 2017) and that two major calving events of Arneb Glacier occurred between 1989–1999 and 2014–2015. No information is available for Edisto Glacier.

3. Data sets and methods

The Edisto Inlet is investigated by integrating several data sets acquired in the frame of different projects funded by the PNRA (Italian Antarctic Research Programme), including sub-bottom profiles, multi-beam bathymetry, gravity and piston sediment cores, Acoustic Doppler Current Profiler (ADCP) data, Conductivity Temperature Depth (CTD) vertical profiles, and thermo-salinograph data.

Sub-bottom profiles were acquired in the fjord entrance using a 3.5 kHz SBP GeoAcoustics Geopulse 5430-5210A on N/R Italica in 2002–2005 with the Seismic acquisition platform (Corradi et al., 2003; Corradi et al., 2009) and a hull-mounted Benthos CAP -6600 Chirp II Data Sonics aboard the RV OGS Explora in 2017 along the entire fjord (Fig. 2). The chirp sweep had frequencies between 2 and 7 kHz with a
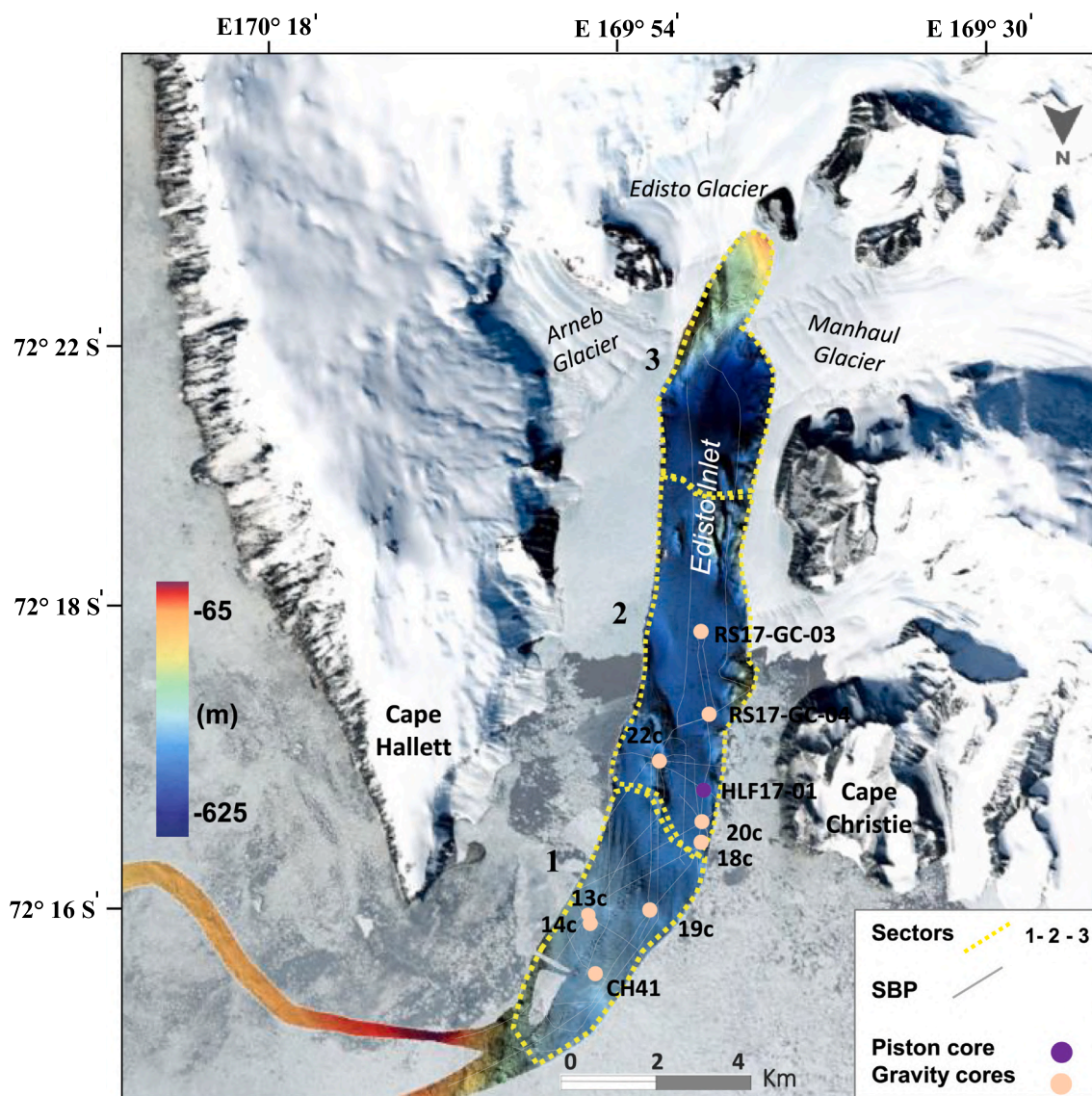

Fig. 2. Map showing multibeam swath bathymetry of Edisto Inlet fjord. Colours scale meters: High 60 m and Low 670 m. Grey lines are the Sub-bottom seismic profiles recorded across the fjord. Orange dots show sediment core locations and purple dot the single piston core. Dashed yellow lines delineate the three sectors of the fjord from 1 to 3 in a north-south direction. (For interpretation of the references to colour in this figure legend, the reader is referred to the web version of this article.)

length of 10 ms, and a tapering function of 10% was used to reduce the magnitude of the Klauder wavelet side lobes (Gutowski et al., 2002a, 2002b).

The Benthos Chirp data, after cross-correlation with the sweep, were recorded in full-wave format rather than Hilbert transform envelope format so that the signal-to-noise ratio could be improved by post-processing (Quinn et al., 1997; Baradello, 2014) to mitigate ocean wave effects and signal ripples. The chirp data from Geopulse were instead acquired in envelope mode, and the pseudo-seismic procedure was performed before standard processing (Baradello et al., 2021).

The two seismic datasets span a wide range of penetration depths (up to 130 ms below the seafloor, corresponding to about 100 m at an assumed velocity of 1500 m/s) (Hamilton, 1979) and vertical resolution between 30 and 10 cm, providing a high-resolution picture of the seismic stratigraphic architecture below the seafloor and good potential for correlation with the main density shift detected in the sediment cores.

The sub-bottom profiles were analysed using the seismic interpretation software IHS Kingdom Suite.

Bathymetric data from the multibeam echo sounders were acquired using a Teledyne Reson SeaBat 7150 multibeam echo sounder with a system frequency of 12 kHz and 880 beams. This dataset was processed with PDS2000 and manually edited to remove anomalous readings, and finally rasterized (20 m resolution) to produce relief maps (Fig. 2).

Nine gravity cores (13c, 14c, 18c, 19c, 20c, 22c, ANTA02-CH41, RS17-GC-03, GC-04) and one piston core (HLF17–01) were studied (Fig. 2). Gravity cores were recovered in the framework of Glaciology and Paleoclimatology, BAY and GLEVORS PNRA Projects in 2002, 2005 and in 2017 and the piston core was recovered in the framework of the HOLOFERNE project in 2017. Core data are detailed in Table 1. Core ANTA02-CH41 was previously analysed by Finocchiaro et al., (2005), cores BAY05-20c was analysed by Mezgec et al. (2017) and Di Roberto et al. (2019) and core HLF17–01 was analysed by Tesi et al. (2020).

Details about the analysis for the sediment cores are given in Table 1 and in the following section and radiocarbon dates on Tables 2.

All the cores are stored at the Sorting Center of the Italian National Antarctic Museum Section of Trieste (available at http://www.mna.it/collezioni/antarctic-marine-sediments-trieste-section).

3.1. Sedimentological analyses

X-radiographic images (X-Ray) were run on all the sediment cores. Multi-Sensor Core Logger (MSCL) measurements were run on cores RS17-GC-03 and GC-04 and the magnetic susceptibility (MS) was measured also on cores 13c, 14, 18c, 19c, 20c and 22c on board with Bartington MS2C. Weight Wt% Total Organic Carbon – (TOC) measured with the FISONS NA2000 Element Analyzer and wt% of Biogenic silica (BioSi) content determined through a progressive dissolution method (DeMaster, 1981), followed by colorimetric analysis acquired in 2005. NaOH 0.5 M was used as an extractant in view of the significant concentrations of biogenic silica usually found in Antarctic samples (DeMaster, 1981). Samples were treated for grain size analyses with hydrogen peroxide to remove organic matter and sieved to separate the <1 mm fraction. The analyses were performed on the cores ANTA02-CH41, BAY05-18c, 20c, and 22c at University of Trieste. The grain size characterization of <1 mm fraction was analysed using a Malvern MasterSizer 2000 laser. Sand, silt and clay were determined using the grain size classification proposed by Friedman and Sanders (1978).

3.2. Oceanographic data

During the 2017 campaign on board RV OGS-Explora, the following along-track data were acquired on the 17th of February: 1) surface temperature and salinity from SBE21 and SBE38 SeaCAT Thermo-salinograph at 4 m depth; and 2) vertical profiles of currents from a RDI Teledyne 75 kHz Vessel Mounted-Acoustic Doppler Current Profiler

Table 1
PNRA sediment cores dataset available in the Edisto Inlet.

PNRA Expedition	Tool	Core ID	Lat (S)	Long (E)	Water depth (cm)	Recovery (cm)	MS Bartington	MSCL	X-ray	Water content	Grain size	TOC	BioSi	PROJECT	References
XVII	gravity core	ANTA02-CH41	72° 17.49'	170° 09.05'	416	406	X		X	X	X	X	X	Glaciology and Paleoclimatology	Finocchiaro et al (2005)
XX	gravity core	BAY05-13c	72° 17.64'	170° 08.92'	411	166	X		X					BAY	
XX	gravity core	BAY05-14c	72° 17.66'	170°08.92'	411	452	X		X	X				BAY	
XX	gravity core	BAY05-18c	72° 17.85'	170° 05.27'	464	419	X		X	X	X	X	X	BAY	
XX	gravity core	BAY05-19c	72° 17.68'	170° 07.48'	422	73	X		X					BAY	
XX	gravity core	BAY05-20c	72° 18.30'	170° 04.46'	456	445	X		X	X	X	X	X	BAY	Mezgec et al. (2017), Di Roberto et al. (2019)
XX	gravity core	BAY05-22c	72° 19.17'	170° 04.83'	447	389	X		X	X	X	X		BAY	
XXXIII	piston core	HLF17–01PC	72° 19.44'	170° 01.58'	465	1465	X		X	X	X	X		HOLOFERNE	Tesi et al. (2020)
XXXIII	gravity core	RS17_GC-03	72° 20.60'	170° 01.11'	495	430		X	X					GLEVORS	
XXXIII	gravity core	RS17_GC-04	72°19.75'	170° 01.11'	504	406		X	X					GLEVORS	

Table 2
Dated horizons using AMS and tephra layer.

Core ID	Depth (cm)	Type of sample	ID Lab	Dating method	Age (yr BP)	Error (yr)	Modelled median age	Minimum 95%	Maximum 95%
ANTA02_CH41	1	Bulk OC	GX-29188	^{14}C	1790	± 40	142	0	372
ANTA02_CH41	35	Bulk OC	GX-30574	^{14}C	4490	± 50	2982	2658	3376
ANTA02_CH41	71	Bulk OC	GX-29991	^{14}C	9400	± 40	8576	8227	8970
ANTA02_CH41	232	Bulk OC	GX-29189	^{14}C	9970	± 50	9287	8896	9648
ANTA02_CH41	300	Bulk OC	GX-29190	^{14}C	10,920	± 50	10,475	10,147	11,008
ANTA02_CH41	369	Bulk OC	CX-29992	^{14}C	9130	± 40	8267	7929	8581
ANTA02_CH41	402	Bulk OC	GX-29191	^{14}C	10,070	± 50	9400	9004	9794
BAY05-18c	1	Bulk OC	OS-75006	^{14}C	2430	± 40	660	403	963
BAY05-18c	67	Bulk OC	OS-75007	^{14}C	4940	± 40	3524	3169	3926
BAY05-18c	175	Bulk OC	OS-75008	^{14}C	8070	± 55	7265	6857	7512
BAY05-18c	284	Bulk OC	OS-75155	^{14}C	11,500	± 75	11,113	10,856	11,831
BAY05-18c	345	Bulk OC	OS-59379	^{14}C	11,550	± 50	11,430	11,008	11,884
BAY05-18c	353	Bulk OC	OS-39370	^{14}C	33,500	± 260	35,650	35,296	36,568
BAY05-20c	2	Bulk OC	OS-59367	^{14}C	1760	± 30	recent		
BAY05-20c	140	Sediment		tephra	650–780		1254[a]		
BAY05-20c	147	Bulk OC	OS-59368	^{14}C	2760	± 40	994	682	1275
BAY05-20c	240	Mollusc	OS-59019	^{14}C	2640	± 30	1409	1116	1708
BAY05-20c	369	Bulk OC	OS-59369	^{14}C	4750	± 30	3289	2929	3678
BAY05-22c	1	Bulk OC	OS-65603	^{14}C	1610	± 35	recent		
BAY05-22c	197	Bulk OC	OS-65787	^{14}C	4700	± 45	3329	2857	3612
BAY05-22c	335	Bulk OC	OS-65599	^{14}C	8150	± 60	7296	6942	7584
BAY05-22c	384	Bulk OC	OS-65806	^{14}C	9000	± 55	8152	7782	7432
RS17-GC03	430	Forams	OS-13138	^{14}C	1940	± 55	714		
HLF17_01	136,5	Sediment		tephra	687	± 7	687[a]	675	698
HLF17_01	1456	Bulk OC	Poz-92,969	^{14}C	4220	± 50	2623[b]	2353	2868

[a] Di Roberto et al. (2019).
[b] Tesi et al. (2020).

(vmADCP), in the range 24–600 m depth with a vertical resolution of 16 m. The vmADCP data were then processed with the CODAS3 software developed by the University of Hawaii (https://currents.soest.hawaii.edu/docs/adcp_doc/). During the 2020 campaign on board PV Laura Bassi, conductivity-temperature-depth (CTD), using a Sea-Bird Scientific SBE911 probe and Lowered-ADCP (LADCP) casts were acquired on the 6th of February along the whole water column at 6 stations in the Edisto Inlet. Thus, simultaneous temperature (expressed in terms of potential temperature), salinity, and current profiles were obtained.

3.3. Chronology

Radiocarbon dating of bulk organic matter sediment for seven cores in Edisto Inlet (CH41, BAY05 18c, 20c, 22c, HLF17–01 and RS17-GC-03) (total ^{14}C n = 21) and carbonate samples (n = 2) was performed via accelerated mass spectrometry (AMS) at The National Ocean Sciences Accelerator Mass Spectrometry (NOSAMS) of the Woods Hole Oceanographic Institution, USA and at the Poznan Radiocarbon Laboratory (Poland).

Given the limitations of using surface sediments to estimate the local reservoir effect (Mezgec et al., 2017) due to the younger age of some cores at the sub-surface, conventional ^{14}C data were corrected for a reservoir age of ΔR_{OC} 1320 ± 135 years developed using an integrated approach by Tesi et al., 2020. The corrected dates were then converted into calibrated age using median calendar ages values (years before present) with the Bayesian program OxCal v4.4.4 Bronk Ramsey (2001), Marine13 calibration curve (Reimer et al., 2013).

With the exception of three dates measured in core Anta02-CH41, which do not quite agree with the above values due to an inversion date, a progression of age down cores is observed (Table 1). Only part of the difference can also be attributed to reproducible variability (Andrews et al., 1997; Andrews et al., 1999). It is more likely that the inversion is due to the release of ^{14}C-depleted glacial meltwater, a time-varying reservoir effect (Van Beek et al., 2002), or contamination during subsampling. Due to the low accuracy and limitations of the model these three dates were not used for the chronological paleoclimatic reconstruction of the fjord.

Other data used in the age-depth model include a tephra layer

recently found in Edisto Inlet sediments, from eruption of Mount Rittmann volcano (Di Roberto et al., 2019). The age of 1254C.E. tephra (and consequently of the BAY05-20c/139–140 and HLF17–01/136,5 crypto-tephra), has been determined also by glacial proxies in Talos Dome (696 ± 2 yr BP; ice record) (Narcisi and Petit, 2021), in the core of Taylor Dome (709 ± 71 yr BP; ice record) (Hawley et al., 2003), and in the core of the West Antarctic Ice Sheet (WAIS) Divide cores (687 ± 7 yr cal BP) (Di Roberto et al., 2019).

4. Results

4.1. Geomorphology

The geomorphology of the seabed shows a maximum water depth of 700 m in the innermost area and a minimum water depth of 100 m near the entrance of the fjord. The fjord was divided into 3 sectors (Fig. 2) with different morphological characteristics. Sector 1 is the shallowest, at the entrance of the fjord. It has streamlined, parallel grooves and ridges in a water depth of 410–470 m (Fig. 3b, c). The streamlined grooves are, on average, between 1 and 3 km long, 100–200 m wide, and several tens of meters high. They show a distinct alignment parallel to the fjord axis, indicating the direction of ice flow, and terminate toward sector 1 in correspondence with a wedge-shaped depositional system with a relief of ~15 m toward the north (Fig. 3b, d). A smooth and nearly flat seafloor with isolated ridges up to 60 m high and steep flanks characterize Sector 2 in the centre of Edisto Inlet (Fig. 3a).

The southern sector of the fjord, sector 3, in front of Edisto Glacier is dominated by a depression up to 670 m deep (Fig. 3e). An arcuate ridge crossed by channels is located in about 500 m of water depth, in front of Manhaul Glacier (Fig. 3 e). The western flank is characterized by ridges in a west-east direction, ranging from 100 to 300 m wide, with a relief of 1–2 dozen meters, bounded by channels (Fig. 3f, g). Ridges with relief of 1 to 2 dozen meters, running east-west and north-south and bounded by gullies, characterize the southern shallow water area of Sector 3 (Fig. 3f). A shallower and smoother seabed characterizes the eastern area of Sector 3.
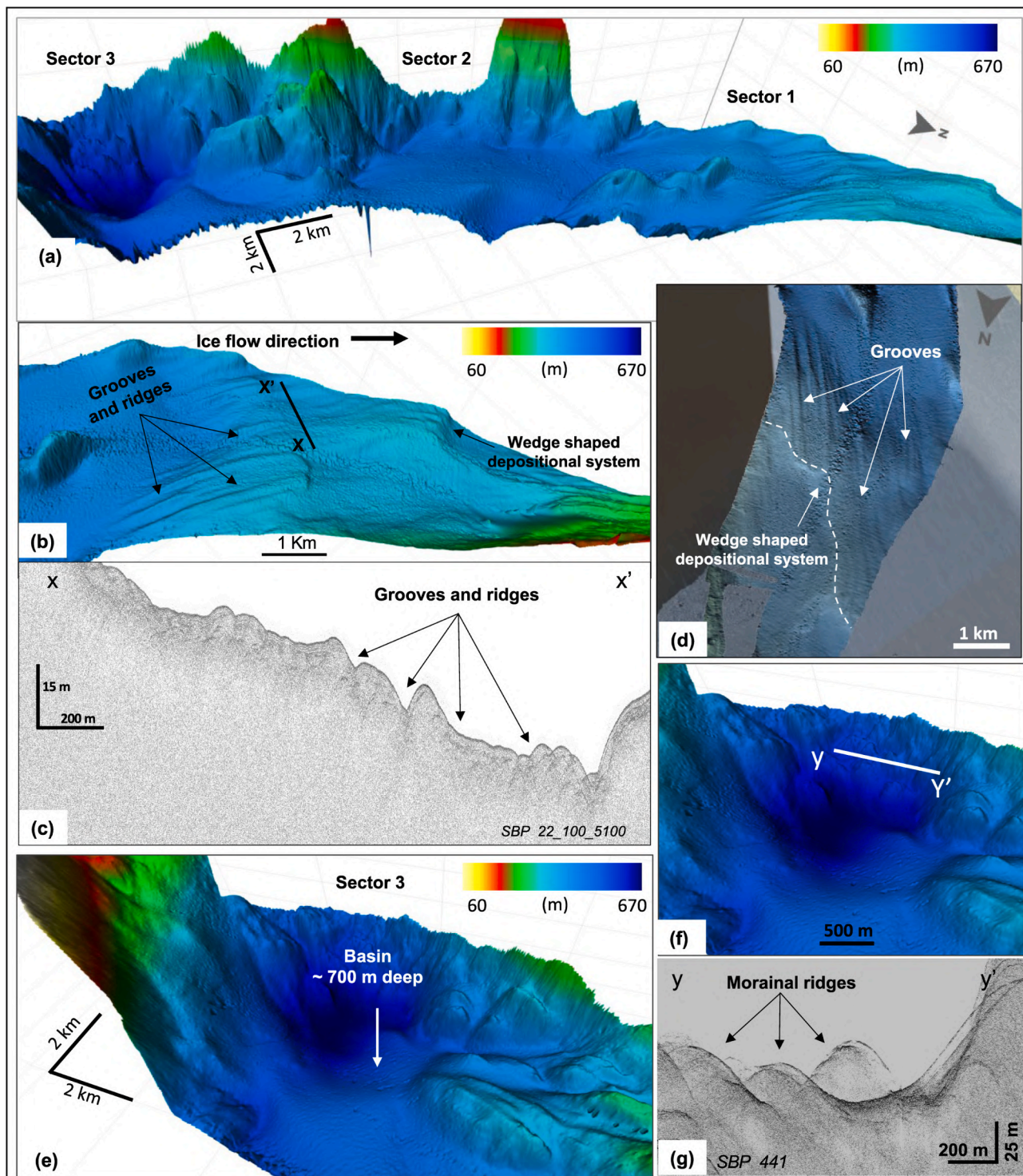
Fig. 3. Multibeam echosounder bathymetry of Edisto Inlet fjord in a 3D representation of the fjord with bedforms (a). The flow direction of the paleo-ice and the parallel grooves to the north are shown (b, c, d). In d the white dotted line is the limit of the scarp depositional system. The southernmost sector of the fjord shows a wide and deep depression (maximum depth about 670 m) (e). Location in (b, f) and cross-sectional profiles X – X' (c), Y – Y′ (g) show the morphology of grooves and moraine ridges bounded by channels. The colour bar is in metres.
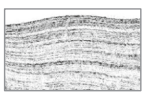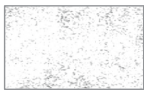
4.2. Seismic facies

The sedimentary sequence in Edisto Inlet fjord, mapped using sub-bottom data, is divided into two main seismic facies, referred to as EI and EII (Table 3). The EI seismic facies consists of laterally continuous, high-amplitude stratified reflectors, that generally conform to the sea-floor. Locally, the seismic reflectors of facies EI are undulating or convex and converge, pinching out laterally and becoming discontinuous beneath morphologic moats. The EI unit thins in Sectors 1 and 3, reaching a maximum thickness of 150 milliseconds (ms) TWT in the central part of the fjord in Sector 2 (a minimum of 110 m assuming a velocity of 1500 m/s).

Seismic facies EII is located below facies EI. It is transparent with no internal organization overlying the acoustic basement and is up to 50 ms

Table 3
Seismic facies legend of the study area.

Seismic facies classification				
Facies Unit	Seismic Example	Internal configuration	Amplitude	Lateral continuity
Facies EI		Sub horizontal to undulated stratified reflections	High to medium amplitude	Good lateral continuity
Facies EII		Transparent with no internal organization	Low amplitude	Low lateral continuity

(two-way travel time) thick, corresponding to a thickness of at least 35 m (assuming a seismic wave velocity of about 1500 m/s within the sediments) in the northern and central part of the fjord. Facies EII is not observed in the southern sector. Here it may not be present or may be deeper than the penetration depth of the seismic system used in this work.

4.3. Sedimentary facies

Physical properties, grain size data, biogenic silica (BioSi), total organic carbon (TOC), and X-rays support the presence of three main sedimentary facies: a glacimarine, diamicton facies *(GDf)*, a marine, laminated facies *(Lf,)*, a marine, massive bioturbated facies with gravel *(MBf)*, and two sub-facies a strongly laminated sub-facies *(SL -sf)* and weakly laminated sub-facies *(WL -sf)*. Facies *GDf* was deposited during the LGM; facies *Lf* (and subfacies *SL-sf and SL-wf*) and *MBf* were deposited after the LGM in Sectors 1 and 2 of the fjord. These facies provide direct lithologic information (Table 4) for the acoustic facies identified on the seismic profiles. No sediment samples are available from Sectors 3.
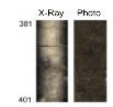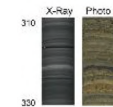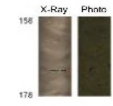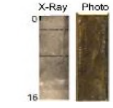
Fig. 4 summarizes the characteristics of drill core BAY05-18c, which is characterized by most of the recognized facies, while the other drill cores are shown in Fig. S1 in Supplementary.

The *Glacimarine Diamicton facies (GDf)* is characterized by high dry density and high magnetic susceptibility (Table 4). It is a massive, dark olive-colored sediment with numerous pebbles in a sandy silt matrix. Water content, TOC and BioSi content are lower than in the other facies. Biogenic material is not present. This facies is found at the bottom of cores BAY05-14c in Sector 1 and BAY05-18c in Sector 2. Its age is >35 ka in core BAY05-18c. In both cores, the facies is bounded by an upper sharp contact. The *GDf* facies is also present at the bottom of core BAY05-22c in Sector 2 and is dated at >8 ka BP.

Laminated facies (Lf) is characterized by diatom ooze with low clastic material, and it is subdivided in two sub-facies:

- The *strongly laminated subfacies (SL -sf)* has very low MS and dry density, high water content and BioSi (average 33%), and about 0,62% of TOC. The laminae are regularly parallel and are characterized by an alternation of dark (very dark grey to black) and light (pale olive/olive to olive grey) colour. The light colour corresponds to a diatom ooze, while the dark laminae also have a clastic (volcanoclastic) component. Carbonate fragments are present but rare in the *SL -sf subfacies*, except for the bottom of the core RS17-GC-003, where the discrete presence of foraminifera has allowed radiocarbon dating. The contact with the overlying facies is gradual. This subfacies is present at the base of core ANTA02-CH41, overlies facies *GDf* in cores BAY05-14c and BAY05-18c, and is the only facies in cores BAY05-20c, HLF17–01, and RS17-GC-03 and RS17-GC-04. This subfacies was deposited between about 10 and 11.4 ka in Sector 1 and since the last 4 ka in Sector 2.

- The *weakly laminated subfacies (WL -sf)* has a higher MS than SL -sf, a lower water content, and a similar TOC content to *SL -sf*. In this subfacies, the laminae are similar to those in the *SL -sf subfacies*, but they are not regular and sometimes massive structure predominates. The colour varies from olive to dark olive grey. Carbonate fragments are rare and some millimeter to centimeter sized clasts are present. Contact with overlying facies is gradual. A tephra layer is present in this subfacies in cores BAY05-20c and HLF17–01 (Di Roberto et al., 2019; Tesi et al., 2020). The *WL -sf subfacies* overlies the *SL -sf subfacies* in ANTA02-CH41, BAY05-14c, and BAY05-22c, the latter characterized by intense bioturbation. The *WL -sf subfacies* was

Table 4
Summary of facies affiliation of the studied cores.

Facies association	Lithology	Sedimentary structure	Physical and geochemical properties	Environmental Interpretation	Representative photos of facies association
GDf	Gravel-rich sediment with abundant pebbles in a sandy silt matrix	Massive, chaotic	MS: 7087 x10⁻⁶ SI; water content: 27%; dry density: 0,755g/cm³; sand/silt/clay: 14/81/5%; TOC: 0,41%; BioSi:10%	Glacimarine Diamicton	
SL-sf	Alternance of diatom ooze and more clastic sediment laminae	Crudely laminated	MS: 301 x10⁻⁶ SI; water content: 80%; dry density: 0,236g/cm³; sand/silt/clay: 14/81/5%; TOC: 0,62%; BioSi: 33%	Low energy open marine condition with a seasonal alternation of productivity events	
WL-sf	Sandy silt light to dark laminae of diatoom ooze	Massive to weakly laminated	MS: 2861 x10⁻⁶ SI; water content: 59%; dry density: 0,552g/cm³; sand/silt/clay: 23/65/12%; TOC: 0,66%; BioSi: 19%	Medium to low energy open marine conditions with more persistent sea ice coverage	
MBf	Silty sand to sandy silt coarse grained sediment with dispersed gravel clasts	Massive, bioturbated	MS: 9180 x10⁻⁶ SI; water content: 39%; dry density: 0,929g/cm³; sand/silt/clay: 41/53/6%; TOC: 0,45%; BioSi: 7%	Meltwater facies linked to strong bottom tidal currents	

The *GDf* facies is represented here by the interval 381–401 cm of core BAY05-18c, the sub-facies *SL -sf* by the interval 310–330 cm of core ANTA02-CH41; the sub-facies *WL -sf* by the interval 158–178 cm of core BAY05-22c; the facies *MBf* by the interval 0–16 cm of core BAY05-18c. Physical and geochemical properties are given as average values, except for BioSi of *WL -sf*, for which only a single value is available.
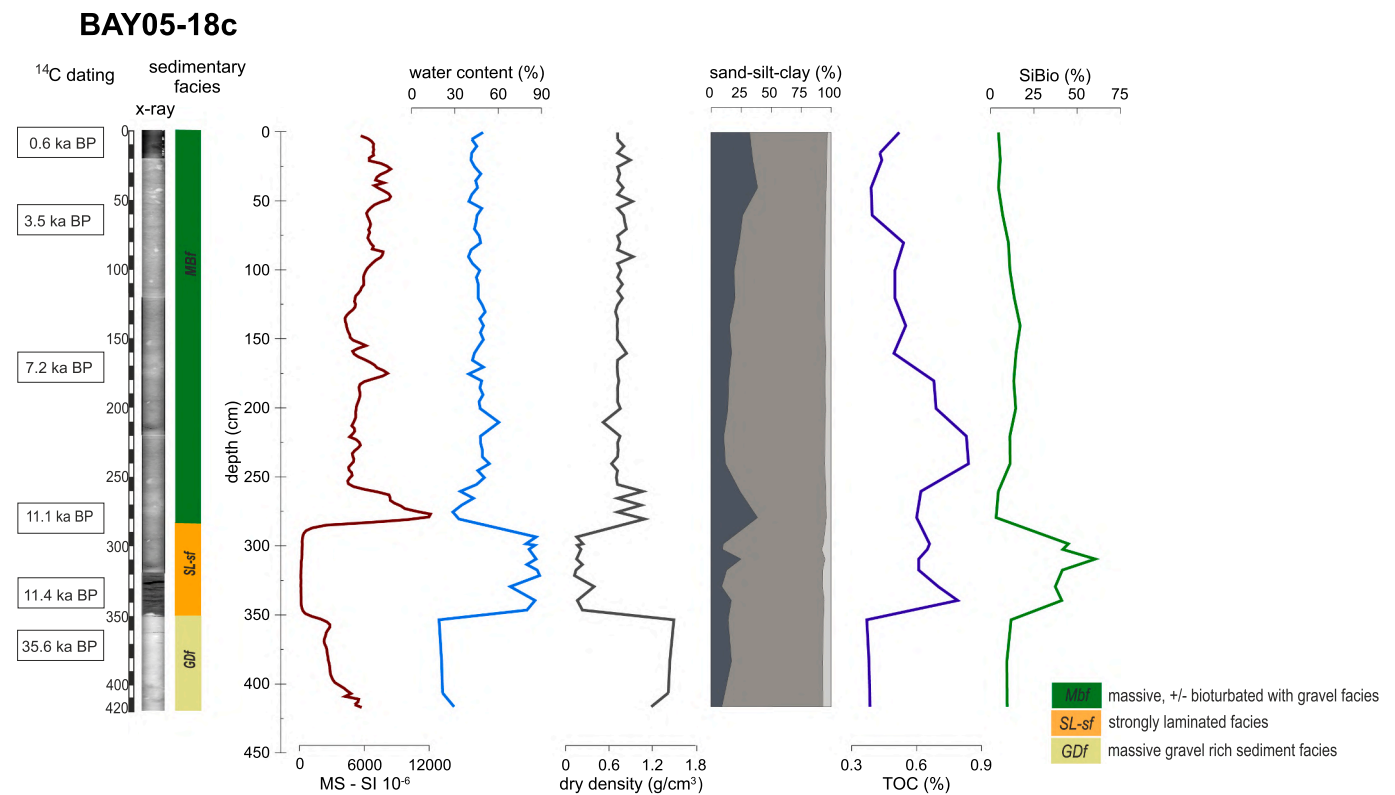
Fig. 4. Fig. S4: Summary of X-ray, magnetic susceptibility (SI), % water content, dry density, % grain size, % TOC, and % SiBio curve from core BAY05-18c. Lithitologic facies are given as follows: *GDf* = glaciomarine diamicton facies (in light green), *SL -sf* = strongly laminated subfacies (orange), *WL -sf* = weakly laminated subfacies (yellow) *MBf* = massive, bioturbated facies with gravel facies (green). (For interpretation of the references to colour in this figure legend, the reader is referred to the web version of this article.)

deposited in a short time interval of about 9–9.4 ka in Sector 1, while the age of the *WL -sf subfacies* in core Bay05-22c ranges from <8 ka to the present.

A *massive bioturbated facies with gravel (MBf)* is a massive, sometimes bioturbated silty sand to sandy silt sediment with scattered gravel clasts. The MS values, which are higher than in the underlying subfacies, also indicate a larger clastic presence. Colour varies from dark olive grey to very dark grey. Contact with the other facies is gradual. This facies occurs at the top of the cores ANTA02-CH41, BAY05-13c, 14c,18c and 19c. It was deposited from 9 ka to present.

4.4. Oceanography

Oceanographic data collected during the 2017 and 2020 cruises are summarized in Fig. 5. They reveal variable surface conditions, and the presence of a double layer stratification in the water column associated with different regimes of current direction and magnitude in upper and deep layers. The horizontal thermohaline distribution at 4 m depth observed in February 2017 (Fig. 5a, b) indicates that the lowest temperature values (of around −1.6 °C) and the highest salinity values (34.27 psu) characterized the innermost part of the fjord (sector 3). Within sectors 1 and 2 of the fjord, six vertical CTD profiles were conducted in February 2020 (Fig. 5c, where the one closest to the location of the core RS17-GC-04 is highlighted). They show that the surface layer is relatively warmer and fresher than the deep one. Temperatures from −1.3 to −1.7 °C were measured in the upper 100 m, while in the deep layer the temperature drops to < −1.8 °C, and the salinity seems uniform (around 34.65 psu). Despite the scarcity of available data, their combination documents the existence of a thermocline/halocline/pycnocline between 50 and 150 m depth, where the water properties gradually change. The largest current speeds, measured by a LADCP

near the core location in February 2020, are found mostly in the upper 100 m depth (Fig. 5d). The contribution of the tidal influence on the current regime and thermohaline distribution is estimated here only for its barotropic astronomical component (Fig. 5e). The flow inside the Bay, observed by means of the vmADCP along the ship track during February 2017 survey, which lasted about 8 h, varies in speed and direction within different sectors and along the entering and exiting route. The magnitude of the horizontal currents ranges between 0 and 0.26 m/s and along most of the route the flow shows a two-layer structure (above and below about 150–200 m, not shown). Along the W-E section (Fig. 5f) we observe markable speed differences between the upper 150–200 m at the W border (speed about 0.10 m/s) and the central part (speed <0.06 m/s). Moreover, the direction of the flow in the upper 150 m is opposite or almost opposite to that measured between 150 and 300 m, but also to that on the eastern flank, where the velocity increases slightly. Furthermore, this snapshot shows that in the central part of the channel, where the velocities are 0.06 m/s, "the sediment deposits are large" (Fig. 5g).

5. Discussion and interpretation

5.1. Evidence of glacial dynamics

Different types of glacial bedforms were found on the seafloor of the fjord. The northward expansion of glaciers within the Edisto Inlet during the LGM is supported by the evidence of the occurrence of grounding ice in the shallowest Sector 1 (Fig. 3b, c) at the entrance to the fjord. Here, the elongate grooves that develop parallel to the fjord axis, are interpreted as glacial lineations generally associated with a deforming till. The asymmetric, wedge-shaped depositional system at the termination of the glacial lineation represents the grounding zone wedge (GZW) (Fig. 3d), as observed in similar glacial settings (Stokes and Clark, 2001;
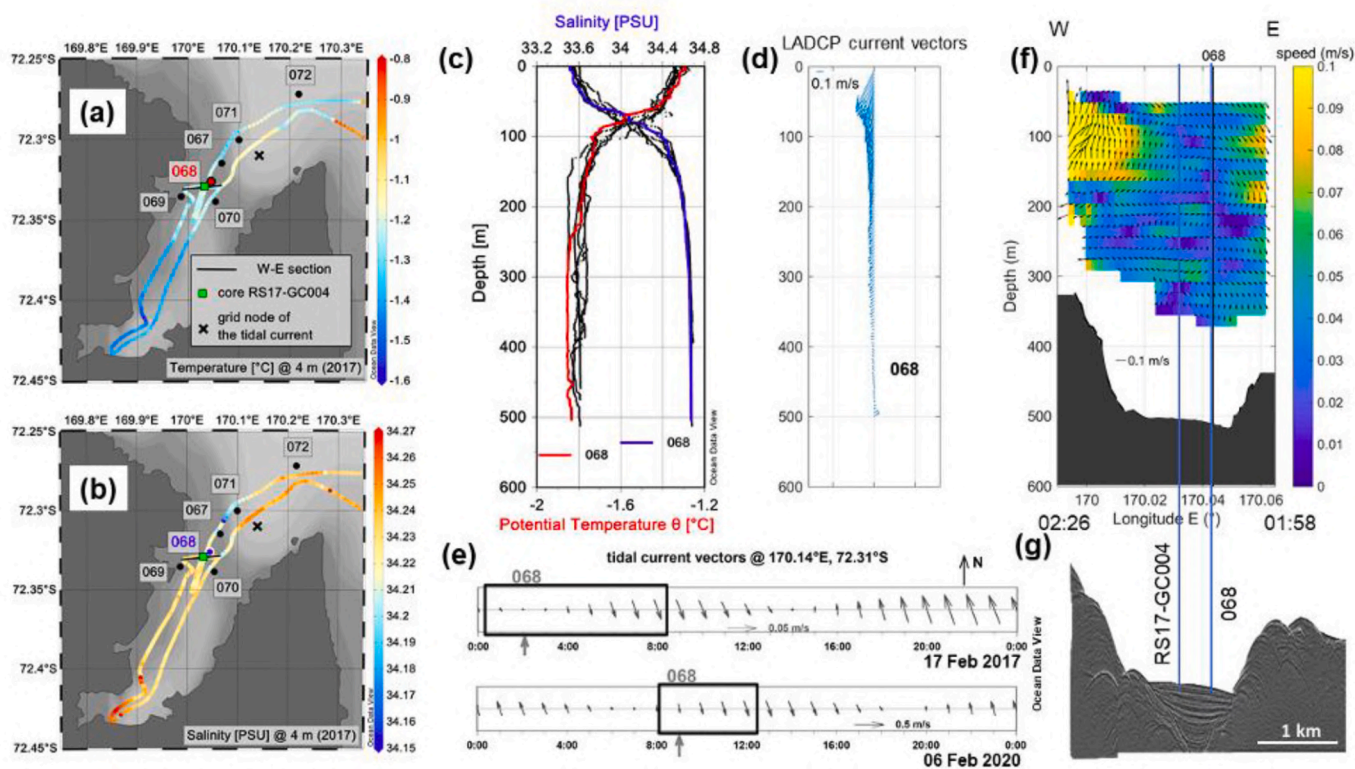
Fig. 5. Oceanographic properties in the Edisto Inlet, based on data acquired in 2017 and 2020.
Temperature (a) and salinity (b) along the ship track at 4 m depth during the survey in 2017; potential temperature and salinity from the six CTD casts in 2020 with emphasis on the 068 cast (c); current vectors from the LADCP at station 068 (d); hourly barotropic tidal current from Tide Model Driver (TMD, Erofeeva et al., 2005) for the duration of the 2017 and 2020 surveys (black rectangles; note the speed scale change between 2017 and 2020), with the times (grey arrows) corresponding to the passage close to station 068 (e); a vertical transect of the currents from the vmADCP (f) and the sub-bottom profile (g) along the section W-E (indicated in a), with positions of the gravity core and 068 CTD. The locations of the selected tidal grid node (in e), the W-E section (in f and g), the gravity core RS17-GC-04, and six CTD/LADCP stations (067–072, in c and d) are indicated in (a). All indicated dates and times are in UTC (coordinated universal time). The northward (N) direction of the current vector is indicated in (e) and is valid for (d) and (f).

Ship et al., 1999, Shipp et al., 2002; Canals et al., 2000; Wellner et al., 2001; Batchelor and Dowdeswell, 2015; Ó Cofaigh et al., 2016; Slabon et al., 2016; Halberstadt et al., 2016). The orientation of the glacial lineations (NE-SW) indicates that they were likely caused by glaciers advancing from Edisto Inlet fjord, rather than the nearby Ironside Glacier or Honeycomb Glacier, which lie outside the fjord.

The deep depression (~670 m depth) in Sector 3 was likely formed during past advances and retreats of the Edisto Glacier and Manhaul Glacier. At the southern end of the fjord is a field of small mounds of transparent deposits with no internal organization, interpreted as residual recessional moraine deposits (Fig. 3g) (Small, 1983; Baroni and Orombelli, 1987; Smith et al., 2019). The channels formed as a preferential conduit of meltwater runoff during glacial retreat. Overall, these glacial bedforms provide evidence that the Edisto Inlet fjord glaciers expanded and retreated in the past relative to their present location.

The *glacimarine diamicton GDf* here is characterized by gravel-rich sediments with pebbles in a sandy silt matrix, indicative of ice-proximal environment. It is commonly observed in continental shelf of the Ross Sea (Prothro et al., 2020) and other glaciated areas (Escutia and Brinkhuis, 2014). The age of the *GDf* recovered at the entrance to the fjord is unknown, but the stratified sediment (facies *SL-sf*) lying above the *GDf* in core ANTA02-CH41 is dated ca. 9 ka (Fig. S2g). The *GDf* recovered at the entrance to the fjord correlates with a high-amplitude seismic reflector within acoustic facies EII (Fig. 6) which can be used to map the occurrence and distribution of the ice proximal sedimentary facies *GDf* in Sector 1 (light green horizon in Fig. 6). The base of facies EII is the acoustic basement and likely represents sediments that were compacted or eroded during the LGM as glaciers advanced across the

entire Edisto Inlet fjord. A similar high-amplitude reflector within facies EII, which correlates with the sharp boundary between sedimentary facies *GDf* dated to 35 ka and facies *SL-sf* dated to 11 ka in core BAY05-18c (light green horizon in Fig. 7), is evident in Sector 2 and can be traced, although discontinuously, southward into the central part of the fjord. Sediment cores collected in the innermost part of the fjord do not reach this reflector, which is about 5–10 ms above the acoustic basement. The acoustic signal from the sub-bottom profiles cannot penetrate deep enough to identify and track this reflector in the southern part of the Edisto Inlet fjord, where it becomes very deep. However, it can be identified across the ridge in Sector 2, within facies EII. We can infer that this acoustic reflector represents the top of glaciomarine diamicton deposited as ice proximal material during the retreat of ground ice from the fjord in Sector 1 (in core BAY05 -14c) and in Sector 2 (BAY05-18c) during the retreat of grounded ice from the fjord. Sedimentary characteristics and old age (> 35 ka) suggest that this deposit resulted from material reworked during the last glaciation. This is a typical condition in the western Ross Sea (e.g., Prothro et al., 2020; Khim et al., 2021).

5.2. Edisto Inlet fjord post-LGM evolution

In sectors 1 and 2, a *strongly laminated layer (SL -sf)* made of a diatom ooze with few IRD (core BAY05-14c, 18c, and 22c) (Figs. 4 and S2 b, e) lies on the glacial-marine deposit *GDf*.

The lithological and geochemical features and the diatom assemblage (Finocchiaro et al., 2005) of the *SL -sf* subfacies in Sector 1 (CH41 and 14c) and in Sector 2 (18c), as well as the regular varve sedimentation, are interpreted as seasonal alternation of productivity events (light
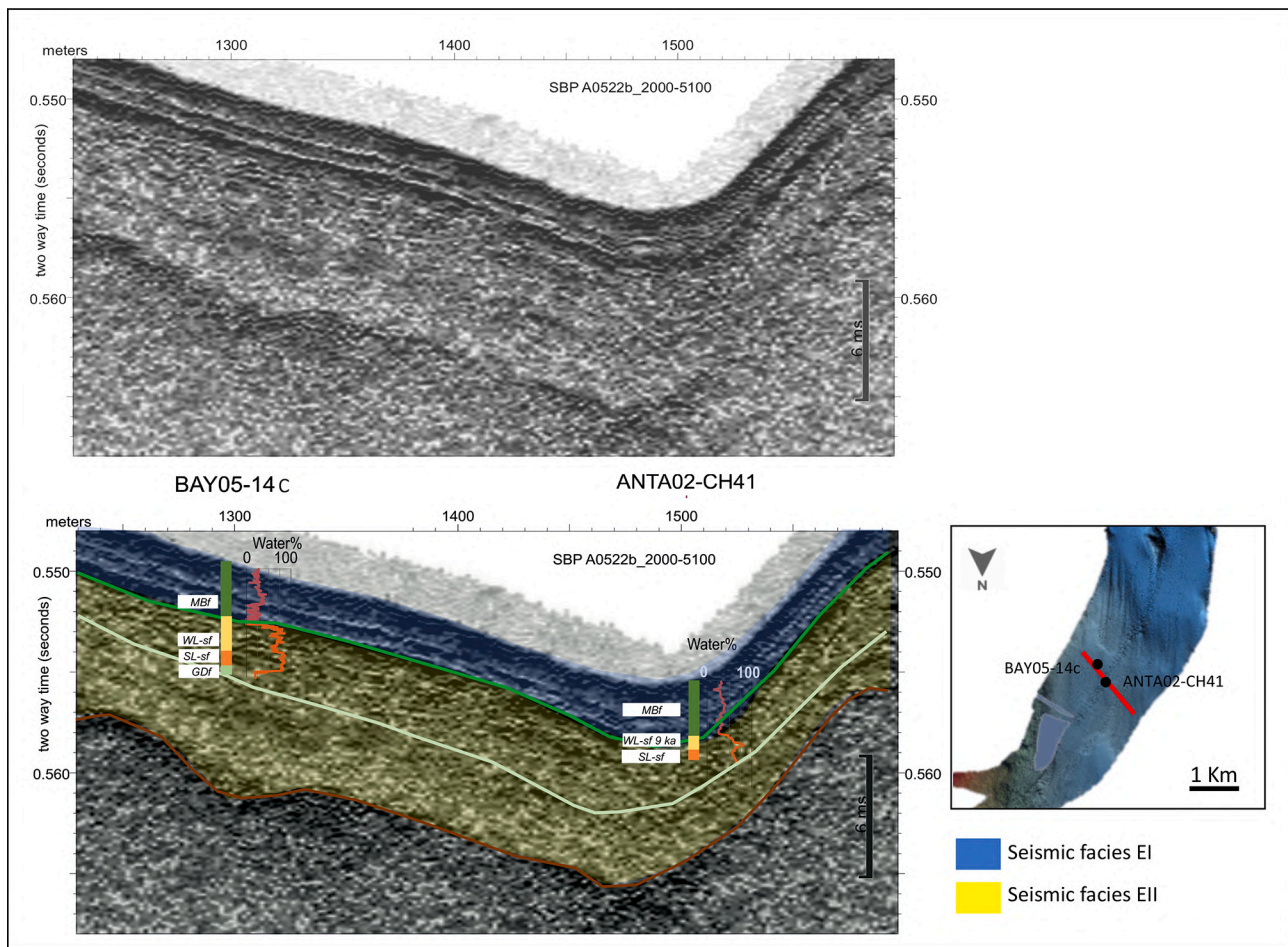
Fig. 6. Subbottom profile number A05sbp22b_2000_5100. The figure shows the correlation between water content (red curve) in sediment cores BAY05-14c and ANTA02-CH41 and seismic reflectors. The light green line highlights the reflector that intersects core BAY05-14c the boundary between the glacial marine diamicton (facies *GDf*) and the stratified sedimentary facies (*SL -sf*), dated to about 9 ka in core ANTA02-CH41. It corresponds with a shift in water content as well as magnetic susceptibility in core BAY05-14c (see also Fig. S2 b, g). The massive sedimentary facies (*MBf*) in the upper part of cores BAY05-14c and ANTA02-CH41 corresponds to layered acoustic facies overlying the green horizon, with a generally low water content, and dated to <8.5 ka. The light brown reflector highlights the acoustic basement, which may represent the base of glacial deposits of the LGM not sampled by any sediment core. (For interpretation of the references to colour in this figure legend, the reader is referred to the web version of this article.)

diatom ooze laminae) and deposition of terrigenous, volcanoclastic debris (dark laminae) deposited in a sluggish or stagnant circulation in open water with low sea ice cover (Cofaigh and Dowdeswell (2001); Leventer et al. (2002); Mugford and Dowdeswell (2011); Lucchi and Rebesco, 2007; Lucchi et al. (2013)).

The abrupt change in sedimentological features (from *GDf* to *subfacies SL -sf*) in cores CH41, 14c and 18c (Figs. 4 and S2 b, g) indicates the onset of open-marine conditions in Sector 1 and 2, dated to ~11 ka. This marks the opening of the sectors 1 and 2 of the fjord after the LGM.

The *SL -sf* is the only facies recorded in Sector 2 and is dated ca. 11 ka in core 18c and 4 ka to present in cores 20c. In core HLF17–01 the very high sedimentation rate (Tesi et al., 2020) and the geochemical and diatom assemblages indicate the establishment of seasonal sea ice alternating with longer periods of open ocean (Mezgec et al., 2017; Tesi et al., 2020).

The *WL -sf subfacies* is found only in Sector 1 cores (CH41-14c) (Fig. S2b,g). Subfacies characteristics indicate a gradual transition to condition of environmental change around 9 and 8 ka, characterized by an increase in bottom current energy (increasing sand content, wavy laminae), while diatom assemblage and decrease in BioSi indicate climate worsening, with the increase of sea ice coverage (Finocchiaro et al., 2005).

Subbottom profiles show that at the southern edge of the Sector 1,

the buried mounds, previously formed as glacial lineations (see section discussed above: "evidence of glacial dynamics") appear imbricated toward the north, within southward dipping thrusts-like structures (Fig. 8). Those thrusts could potentially originate from push-up deformation of soft sediments (*WL-sf* facies and facies *SL-sf*) by the keel of icebergs calving from the south and temporary pinning on the shallow sector 1's southern edge. Gravity flow deposits along the slope between Sector 1 and Sector 2 would originate from the remobilization of the soft material over the edge of sector 1 (Fig. 8). This iceberg calving phase occurred by the end of a cooling interval between 9 and 8 ka. This interpretation is supported by the observation that the glacial lineations imbricated toward north are draped by the non-deformed, well layered acoustic facies EI, and correlated with the sedimentary facies *MBf* dated 8 ka, made of a massive bioturbated and sandy silt sediment layer with sparse ice-rafted debris (*MBf-WL-sf*) at core BAY05-14c, 13c, 19c, CH41 (Fig. 8). Acoustic facies EI and sedimentary facies *MBf* indicate the transition from ice proximal to ice distal in open water conditions, with bottom circulation reinvigoration, ~8–7.2 ka (core CH41, 14c).

Similarly, reconstructions from Wilkes Land, Adelie Land and the Antarctic Peninsula suggest cooling between 10 and 8 ka. Cooling along Wilkes Land and Adelie Land has been linked to glacier advance and sea ice extent (Escutia et al., 2005; Escutia and Brinkhuis, 2014), resulting in a positive feedback on East Antarctic atmospheric temperature. Along
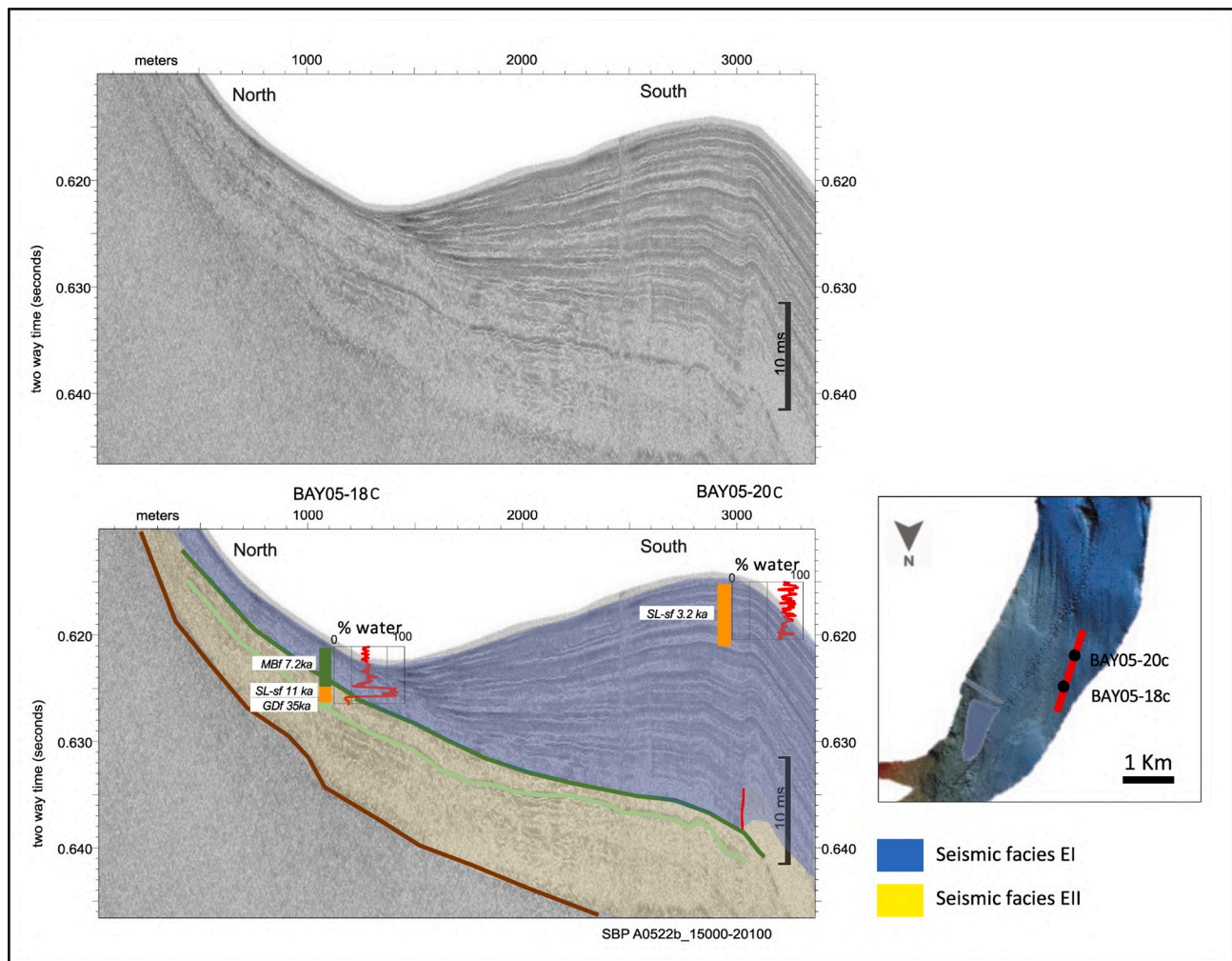
Fig. 7. Subbttom profile number A0522b_15000–20,100. The figure shows the connection of the seismic reflectors with sediment cores BAY05-18c and BAY05-20c. The light green line highlights the reflector that intersects core BAY05-18c at the boundary between the glacial-marine diamicton (facies *GDf*), dated >35 ka and the stratified sedimentary facies (*SL -sf*), dated to 11 ka. It corresponds with a shift in water content and magnetic susceptibility and sediment grain size (see also Fig. 4 and S2 d) and lies at the base of the sedimentary drift that thickens southward within Edisto Inlet. The massive sedimentary facies (*MBf*) in the upper part of core BAY05-18c corresponds to seismic facies EII (semi-transparent), dated >7.2 ka. The green line highlights the reflector that intersects core BAY05-18c at the boundary between the *MBf* and stratified sedimentary facies *SL -sf*. It corresponds to a distinct change in water content (red curve) as well as grain size and magnetic susceptibility (Fig. 4). The green line can be traced southward within Edisto Fjord, where it lies below sediment drift (with seismic facies EI). The brown reflector highlights the acoustic basement, which may represent the base of the LGM glacial deposit and was not sampled by any sediment core. Sediment core BAY05-20c consists entirely of stratified sedimentary facies (*SL -sf*), which has a high-water content, is <3.2 ka in date, and correlates with seismic facies EI (well stratified). (For interpretation of the references to colour in this figure legend, the reader is referred to the web version of this article.)

the Antarctic Peninsula, cooling at 8 ka was suggested to be due to a decrease in south-westerly winds (SW), leading to a decrease in circumpolar deep water (CDW) intrusion onto the continental shelf and subsequent surface cooling (Shevenell et al., 2011). In the Southern Ocean, in the region between the Antarctic Slope Front (ASF) and the Subtropical Front (STF), geologic records generally show intense cooling at 10 to 8 ka, similar to that at the Antarctic surface (Bianchi and Gersonde, 2004; Hodell et al., 2001; Crosta et al., 2005; Nielsen et al., 2004; Pahnke and Sachs, 2006). This shift is believed to be caused by a northward shift of ocean fronts (ACC South Front, Polar Front, Subantarctic Front or STF). In conjunction with this cooling event, diatom records in marine cores south of the polar front suggest a northward migration of the sea ice front during the 10–8 ka period (Nielsen et al., 2004; Bianchi and Gersonde, 2004; Hodell et al., 2001).

5.3. Preserved Late Holocene high-resolution sediment drifts

Sub-bottom data from Sector 2 show exceptionally well-preserved,

undisturbed, bottom current-controlled sediment drifts in the central part of the fjord, consisting of mounded bodies, acoustically stratified (acoustic facies EI) and thinning toward the moats (Fig. 9 They are characterized by a very high sedimentation rate and potentially excellent archives for paleo-oceanographic and paleoenvironmental conditions and provide the opportunity to link ocean, glacial, and climate oscillations (Willmott et al., 2007; Domack et al., 2003). Assuming constant accumulation with a maximum thickness of 110 m in Sector 2 of the fjord, the sedimentation rate is at least twice that reported by Leventer et al. (1993) and Domack et al. (1999) in Granite Harbor and by Dunbar et al. (1989) in McMurdo Sound.

The shape of the drift is controlled by the physiographic environment, which is one of the main factors determining the path and strength of water masses at different depths. Their spatial distribution clearly shows that deposition is also controlled by the physiographic environment. All drift-moats formed on the flanks or behind the ridges. These sedimentary drifts (Fig. 9) have a typical mounded shape with a length of no >2 km and a thickness of >150 ms (110 m) in the middle of the
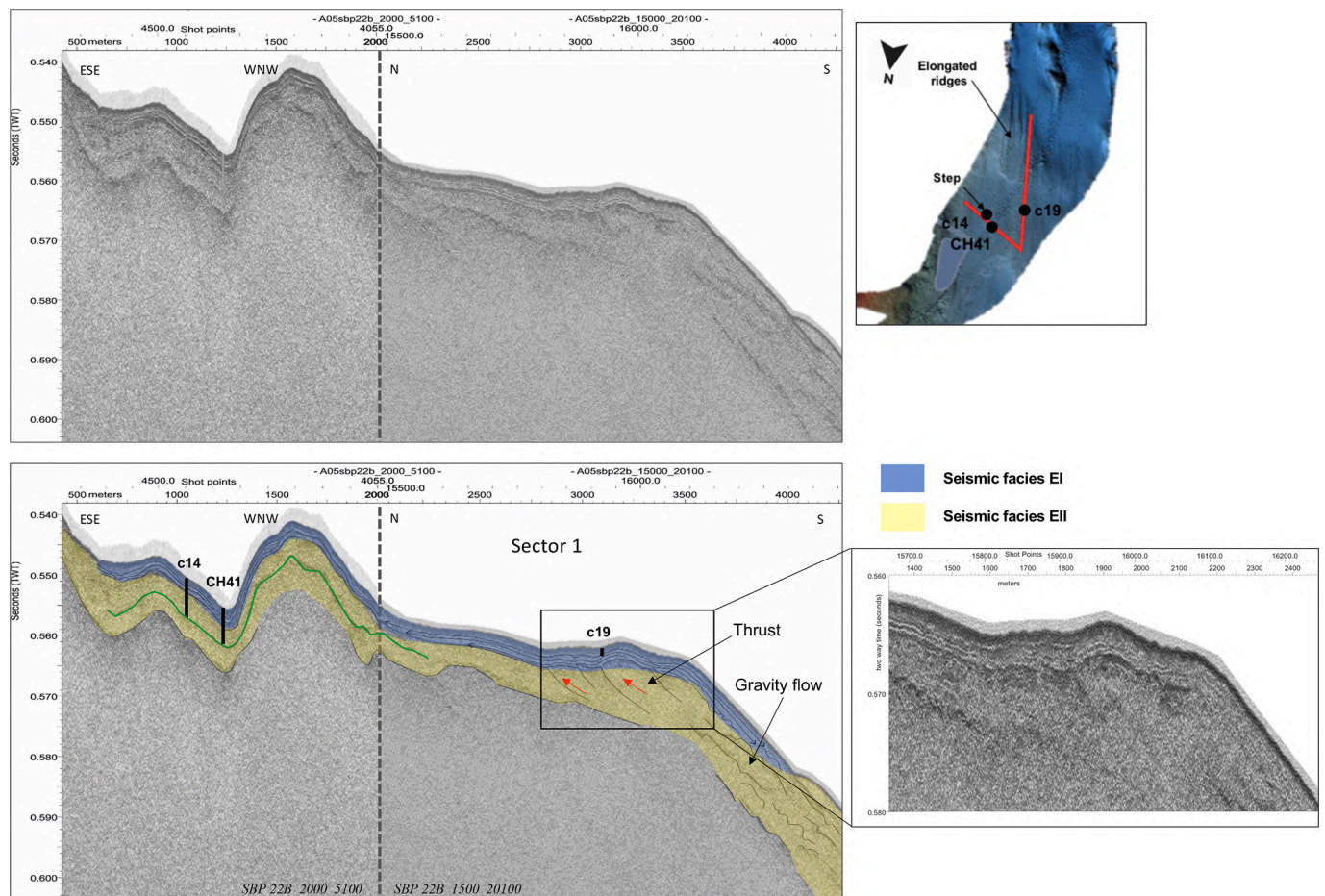
Fig. 8. Seismic lines showing basin floor succession, with the two main seismic facies recognized: EI consists of laterally continuous, parallel, high-amplitude reflections that overlap and dip with seismic facies EII. EII consists of low amplitude opaque or weakly layered, sparse or discontinuous reflections. Gravity deposits occur on the dipping ground beyond the southern margin. Evidence of thrust faulting within seismic facies EII on the right zoom. The light green line highlights the reflector that intersects core BAY05-14c at the boundary between the glacialmarine diamicton (*facies GDf*) and the layered sedimentary facies (*SL -sf*) dated to about 9 ka in core ANTA02-CH41. (For interpretation of the references to colour in this figure legend, the reader is referred to the web version of this article.)

Fjord. (Fig. 10). Some of them are confined drifts (Rebesco et al., 2014a, 2014b), with an arcuate morphology in plan view (Fig. 9). The SBP shows that the main features of the drift in the Edisto Inlet fjord are: 1) a mounded and sigmoidal shape; 2) internal stratification with the reflector eroded or pinching out toward the moat; 3) a moat.

It is often challenging to distinguish whether a stratified depocenter consists primarily of current-driven (contouritic) or gravity-driven (turbiditic) sedimentation processes (Rebesco et al., 2014a, 2016). De Castro et al. (2020) have suggested that contourite drifts do not only result from contourite deposition, but that hemipelagic sedimentation and gravity-driven sedimentation may also contribute to the aggradation of a contourite drift. Alonso et al. (2016), Miramontes et al. (2016) Stow and Smillie (2020), Lobo et al. (2021) have also proposed similar concepts. From these, we infer that the lower part of the Edisto Inlet fjord sediment drift may be interspersed with turbiditic and/or mass flow deposits (chaotic/transparent facies), while the upper stratified part of the drifts is mainly of contouritic origin. The chaotic/transparent facies at the base of the drifts were not reached by sediment cores. The contouritic, well-stratified facies forming the sedimentary drifts is sampled by core BAY05-22c (Fig. S2e). Pervasive bioturbation associated with weak and discontinuous lamination (*WL -sf*) in core BAY05–22c sampled from a sediment drift over a ridge in Sector 2 (Fig. S3) supports the hypothesis of contouritic deposition (Stow and Smillie, 2020). Similar features were also recognized in sediment cores taken on a sediment drift at Kveithola, NW Barents Sea (Rebesco et al., 2016).

The discovery of sediment drifts documents the occurrence of a

relatively long-lived, regular bottom circulation as opposed to episodic events that shape the seafloor. The location of the thickest part of the sediment drift indicates where the current velocity was generally slow, while the moat indicates where the bottom current velocity was high enough to prevent sedimentation.

During the austral summer 2017, LADCP measurements (~400 m depth) showed a good correspondence between the velocity and direction of the bottom currents, the seabed morphology and sediment grain size and the location and shape of the sediment drifts inside the Edisto Inlet fjord. Higher velocities (5 to 30 cm/s) and coarser sediments were measured over moats, lower velocities (< 5 cm/s) and finer grained sediments (BAY05-20c, and BAY05-22c), over the sediment drifts, while very slow circulation occurred in the centre of the fjord where the thickest (up to 110 m), and fine-grained sediments (RS17-GC-03 and 04), are observed.

Oceanographic measurements within the fjord are limited to 2017 ADCP data and a few CTD stations conducted in 2020 at the entrance to the fjord (Fig. 5). More measurements are needed to understand the circulation pattern and the factors that control it, such as winds, sea ice, and tides, which are generally important in narrow fjords. However, the sparsely collected data show water stratification and an apparent gyre inside the interior of the fjord, with a south-south-westward current on the western flank and a north-eastward current on the eastern flank of the fjord.

This is consistent with circulation generally observed in other similarly confined basins, where gyres may transport sediment in
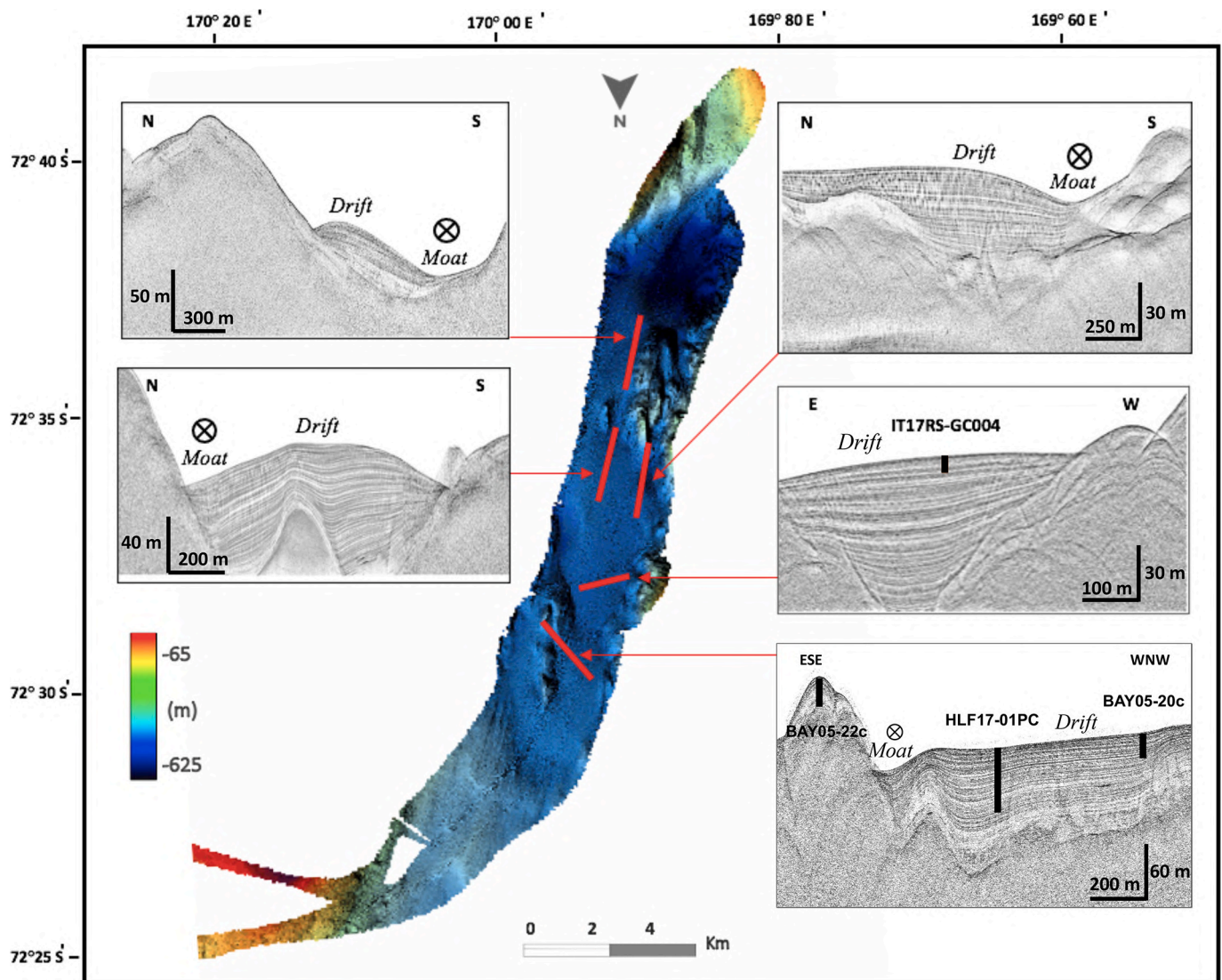
Fig. 9. The multibeam map shows the location of five sediment drifts represented by the SBP profiles (red lines) along Edisto Inlet Fjord. The black lines indicate the location of the sediment cores. The colour bar is in metres. (For interpretation of the references to colour in this figure legend, the reader is referred to the web version of this article.)

suspension, favouring contourite development in sheltered areas (Presti et al., 2005; Rebesco et al., 2016; Neder et al., 2022). According to coupled hydrodynamic models and geomorphologic interpretations for depositional, erosional, and mixed contourite features proposed by Miramontes et al. (2019), separate, elongate drifts develop in the zone where bottom currents are relatively weak, with mean velocities <7 cm/s. Although there are few oceanographic measurements, Edisto Inlet fjord falls into this category based on this evidence.

Lithologic analysis indicates that all the sediment drifts in the Edisto Inlet fjord are made of laminated diatom ooze (*SL-sf and WL-sf facies*). The bottom of the longest drill core (HLF17–01) characterized by the *SL-sf* facies in the upper section of one of the sediment drifts, was dated at 2.62 ka (Tesi et al., 2020) (Fig. S4). Drifts typically form on a time scale of thousands to millions of years (Rebesco et al., 2014b), and our data suggest that their deposition in the Edisto Inlet fjord began at least 8 ka ago (based on the age of the *SL-sf* at the bottom of core 22c) or even earlier (ca. 11 ka, based on the age of the *SL-sf* in core 18c Fig. 4). The deposition and preservation of the thick (110 m) undisturbed sediment drifts in the Edisto Inlet fjord (Fig. 10) can only be explained if a modern-like oceanic circulation with periodic intervals of high productivity, possibly promoted by warm water intrusion, persisted for several

millennia. Ongoing work on the sediment cores is addressing this question. In addition, the preservation of the undisturbed sequence of soft sediments indicates that the glaciers never re-entered the fjord after their retreat.

5.4. Paleoenvironmental reconstruction

During the LGM, the entire Edisto Inlet fjord was carved by glaciers (Fig. 11a). This hypothesis is based on the observation of glacial features in sector 3 and 1 and it is reasonably supported by the small size and depth of the Edisto Inlet fjord considering its large ice catchment area.

We infer that the retreat of the glaciers was gradual, with progressive ice thinning and not interrupted by stationary phases. This is because there is no evidence of grounding zone wedges within the fjord, which would indicate stepwise retreat of the glacier (Simkins et al., 2018; Bart et al., 2017). The morphological sill between Sectors 2 and 3 may have served as a ground ice pinning position in recent times. However, new sediment cores and deeper seismic profiles are needed to confirm this hypothesis.

The glaciers retreated from Sectors 1 and 2 by 11 ka (Fig. 11b). This interpretation is based on sedimentary and acoustic facies observations:
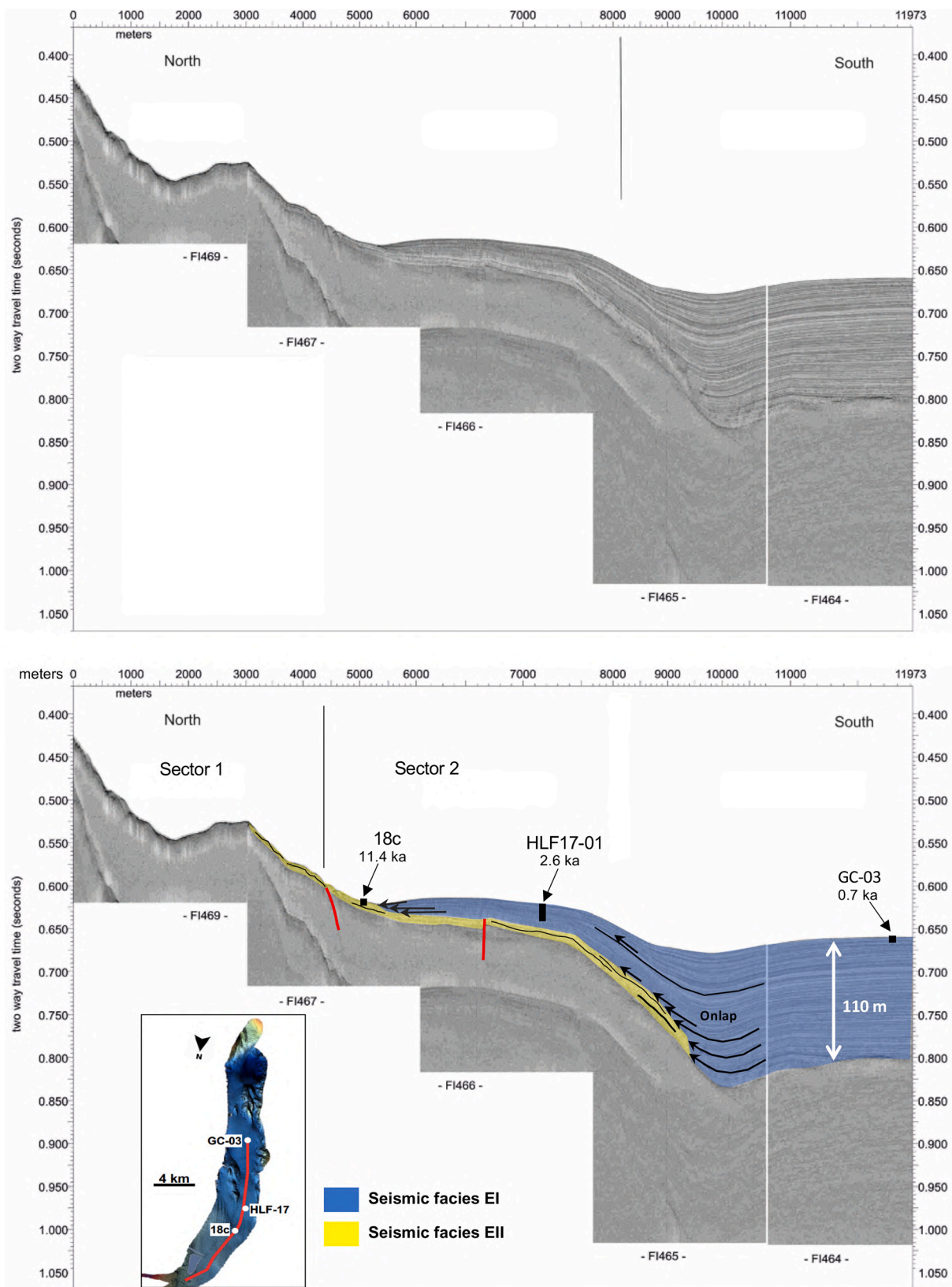
Fig. 10. Sub bottom chirp profiles show elongate sediment drift and a thick (up to 110 m) finely flat stratified unit in Sector 2. The well-stratified parallel reflectors belong to seismic facies EI with convex sigmoidal reflectors terminating in onlap on the top of seismic facies EII or in a pinch-out (black arrows). Seismic facies EII has discontinuous low-amplitude reflections and is up to 35 m thick in the northern and central sectors of the fjord. The red lines indicate normal faults. The black lines show the location of the sediment cores and the calibrated radiocarbon dates at the lower core. (For interpretation of the references to colour in this figure legend, the reader is referred to the web version of this article.)
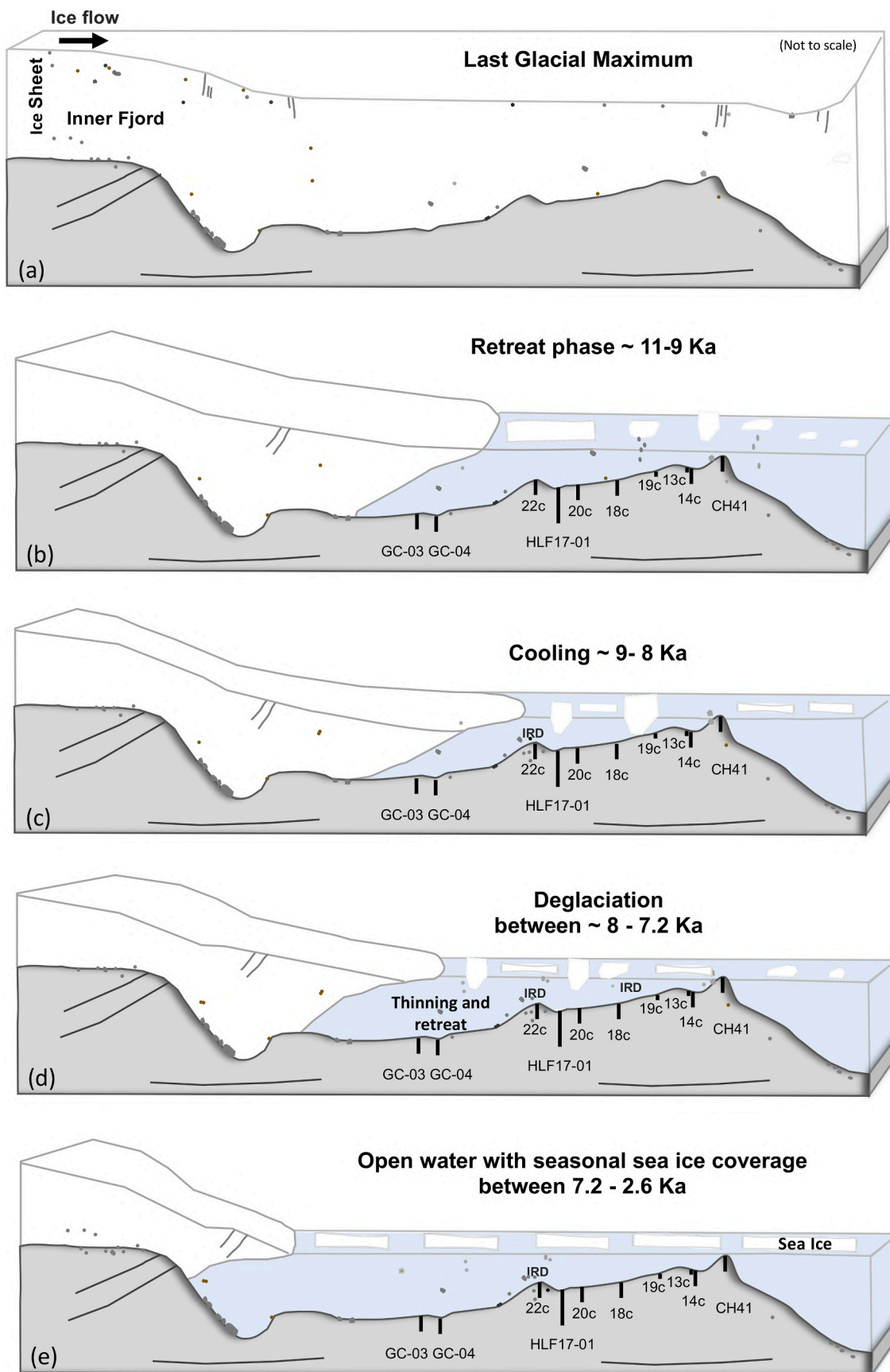
Fig. 11. Schematic diagram showing the progressive opening phases of Edisto Inlet fjord after the LGM. a. LGM. b. Retreat phase between 11 and 9 ka. c. Cooling with iceberg calving between 9 and 8 ka. deglaciation between 8 and 7.2 ka e. Open water conditions with seasonal sea ice cover between 7.2 ka and 2.6 ka. Thereafter, post-modern phase.

1) at this time, the deposition of open water sediments (the biogenic-rich, laminated *SL-sf* sedimentary facies) on top of the ice proximal sediments (the diamicton *GDf* sedimentary facies) in Sector 1 (ANTA02-CH41 and BAY05-14c) and in sector 2 (BAY05-18c) indicates the onset of typical Holocene condition (Finocchiaro et al., 2005). 2) The acoustic reflector corresponding to the base of the *SL-sf* and the top of the *GDf* is a marker that can be recognized and correlated from Sector 1 to almost throughout Sector 2 (Figs. 6 and 8). The acoustic facies and the diatom assemblages of the sedimentary facies *SL-sf* (Finocchiaro et al., 2005) suggest very slow circulation or stagnant conditions in Sectors 1 and 2 (Tesi et al., 2020).

We found evidence of climate cooling and circulation reinvigoration at 9–8 ka (Fig. 11c), from both the sedimentary and the acoustic facies:

1) Weakly laminated and sandy material *(WL -sf)* overlay the *SL -sf* at the entrance to the fjord at about 9–8 ka suggesting a progressive cooling of the fjord's condition. We hypothesize that the sand fraction was likely transported by icebergs, most of which likely originated from further retreat of the Edisto Glacier, floating front, calving during this time period.
2) An evidence in agreement with the hypothesis of the presence of iceberg calving at this time comes from the deformed stratified deposit on the southern edge of the shallowest sector 1 (at about 420 m depth). Such deformation can be explained as probably formed by floating ice drifting northward (Fig. 8).

After this cooling phase, persistent sea ice conditions may have been enhanced by iceberg melting, which increased the stratification of ocean water in the fjord.

A transition to the present-day condition in the Edisto Inlet fjord began around 8–7.2 ka (Fig. 11d) and resulted in the deposition of the massive bioturbated and clast-rich layer *(MBf)* in the outer sector of the bay identified in cores CH41, BAY05-13c, 14c, 18c, and 19c. Undeformed, weakly stratified sediment, deposited under the influence of currents since <8 ka (core 22c), over a ridge within Sector 2 of the fjord.

Cores HLF17_01, RS17-GC-04 and GC-03 suggest that open-marine conditions, with stagnant or very slow current, hemipelagic deposition have persisted in the central sector of the fjord since 2.62 ka ago (Tesi et al., 2020). This is supported by the acoustic facies that show the thickest stratified sediments in the fjord centre (Figs. 9 and 10), while moats occur along the flanks of the fjord, in agreement with a fjord-gyre circulation.

The drift-moats in Sectors 1 and 2 of the Edisto Inlet fjord developed in the course of several thousands of years, sometime between 7.2 ka and 2.6 ka (Fig. 11e). The undisturbed character of all drifts found in the fjord suggests that no glacial advance has occurred since at least 7.2 ka, as indicated by the morphology of the sediment drifts. During this period, the diatom assemblages of Mezgec et al. (2017) and Tesi et al. (2020) support the hypothesis of open – marine conditions.

6. Conclusions

This study shows that the sedimentary sequence deposited in the Edisto Inlet Fjord preserves a unique paleo-oceanographic and paleo-climate record, at millennial resolution, since the LGM. The analysis of seismic, sediment cores and oceanographic data allowed identifying changes in the marine environment that are used to reconstruct five different phases:

- After the Last Glacial Maximum coastal glaciers retreat from the outer and central sector of the fjord. The inner sector of the fjord was likely still covered by grounding ice
- Between 11 ka and 9 years thinly laminated mud filled the fjord in warm, open and stratified water. During this time a marine circulation was established inside the fjord.

- Between 9 ka and 8 ka weakly stratified sediments deposited in a cooling environment with alternation of sea ice cover and open water. During this time the circulation regime slowed comparing to the previous phase.
- around 8–7.2 ka the deposition of massive bioturbated and clast-rich layer indicate acceleration of deglaciation of the coastal glaciers.
- between 7.2 ka and 2.6 ka, drift-moat deposits developed inside the Edisto Inlet fjord indicating persistent circulation

Our results highlight the potential of this region for shallow drilling, to provide an unprecedented record for reconstructing the evolution of northern Victoria Land's glaciers and further studies to predict the evolution of the Antarctic ice sheet and its future contribution to sea level rise.

Declaration of Competing Interest

The authors declare that they have no known competing financial interests or personal relationships that could have appeared to influence the work reported in this paper.

Data availability

Datasets related to this article can be found at DOI: 10.13120/GAS9-6 N43.
doi:10.13120/gas9-6n43 and DOI 10.13120/6r01-ad93 https://doi.datacite.org/dois/10.13120%2F6r01-ad93 an open-source online data repository hosted at National Institute of Oceanography and Applied Geophysics - OGS.

Appendix A. Supplementary data

Supplementary data to this article can be found online at https://doi.org/10.1016/j.margeo.2023.107189.

References

Alonso, B., Ercilla, G., Casas, D., Stow, D.A., Rodríguez-Tovar, F.J., Dorador, J., Hernández-Molina, F.J., 2016. Contourite vs gravity-flow deposits of the Pleistocene Faro Drift (Gulf of Cadiz): sedimentological and mineralogical approaches. Mar. Geol. 377, 77–94.

Anderson, J.B., Conway, H., Bart, P.J., Witus, A.E., Greenwood, S.L., McKay, R.M., Stone, J.O., 2014. Ross Sea paleo-ice sheet drainage and deglacial history during and since the LGM. Quat. Sci. Rev. 100, 31–54.

Anderson, J.B., Simkins, L.M., Bart, P.J., De Santis, L., Halberstadt, A.R.W., Olivo, E., Greenwood, S.L., 2019. Seismic and geomorphic records of Antarctic Ice Sheet evolution in the Ross Sea and controlling factors in its behaviour. Geol. Soc. Lond. Spec. Publ. 475 (1), 223–240.

Andrews, J.T., Smith, L.M., Preston, R., Cooper, T., Jennings, A.E., 1997. Spatial and temporal patterns of iceberg rafting (IRD) along the East Greenland margin, ca. 68 N, over the last 14 cal. ka. J. Q. Sci. 12 (1), 1–13.

Andrews, J.T., Domack, E.W., Cunningham, W.L., Leventer, A., Licht, K.J., Jull, A.T., Jennings, A.E., 1999. Problems and possible solutions concerning radiocarbon dating of surface marine sediments, Ross Sea, Antarctica. Quat. Res. 52 (2), 206–216.

Ashley, K.E., Crosta, X., Etourneau, J., Campagne, P., Gilchrist, H., Ibraheem, U., Bendle, J., 2021. Exploring the use of compound-specific carbon isotopes as a paleoproductivity proxy off the coast of Adélie Land, East Antarctica. Biogeosciences 18 (19), 5555–5571.

Baradello, L., 2014. An improved processing sequence for uncorrelated Chirp sonar data. Mar. Geophys. Res. 35 (4), 337–344.

Baradello, L., Battaglia, F., Vesnaver, A., 2021. Fast method to transform chirp envelope data into pseudo-seismic data. Mar. Geophys. Res. 42 (2), 1–11.

Baroni, C., Orombelli, G., 1987. Indagini geomorfologiche e glaciologiche nella Terra Vittoria (Seconda Spedizione del Programma nazionale di Ricerche in Antartide, 1986-1987). Geograph. Fis. Dinam. Q. 10, 321–336.

Bart, P.J., Anderson, J.B., Nitsche, F., 2017. Post-LGM grounding-line positions of the Bindschadler paleo ice stream in the Ross Sea Embayment, Antarctica. J. Geophys. Res. Earth 122 (10), 1827–1844.

Bart, P.J., DeCesare, M., Rosenheim, B.E., Majewski, W., McGlannan, A., 2018. A centuries-long delay between a paleo-ice-shelf collapse and grounding-line retreat in the Whales Deep Basin, eastern Ross Sea, Antarctica. Sci. Rep. 8 (1), 12392.

Batchelor, C.L., Dowdeswell, J.A., 2015. Ice-sheet grounding-zone wedges (GZWs) on high-latitude continental margins. Mar. Geol. 363, 65–92.

Bentley, M.J., Cofaigh, C.O., Anderson, J.B., Conway, H., Davies, B., Graham, A.G., RAISED Consortium, 2014. A community-based geological reconstruction of Antarctic Ice Sheet deglaciation since the Last Glacial Maximum. Quat. Sci. Rev. 100, 1–9.

Bianchi, C., Gersonde, R., 2004. Climate evolution at the last deglaciation: the role of the Southern Ocean. Earth Planet. Sci. Lett. 228 (3–4), 407–424.

Bronk Ramsey, C., 2001. Development of the radiocarbon calibration program. Radiocarbon 43 (2A), 355–363.

Canals, M., Urgeles, R., Calafat, A.M., 2000. Deep sea-floor evidence of past ice streams off the Antarctic Peninsula. Geology 28, 31–34.

Cofaigh, C.O., Dowdeswell, J.A., 2001. Laminated sediments in glacimarine environments: diagnostic criteria for their interpretation. Quat. Sci. Rev. 20 (13), 1411–1436.

Cofaigh, C.O., Livingstone, S.J., Dowdeswell, J.A., 2016. Mega-scale glacial lineations in Marguerite Trough, Antarctic Peninsula. Geol. Soc. Lond. Mem. 46 (1), 175–176.

Corradi, N., Giordano, F., Giordano, R., 2003. The application of a very High Resolution Hardware-Software (DSeismic) system for the acquisition of seismic data for the study of the Ross Sea (Antarctica) Sedimentary Deposits. In: Proceedings of the Italian Association of Oceanology and Limnology, pp. 115–124.

Corradi, N., Ferrari, M., Ivaldi, R., 2009. SAM sources and the DSeismic system: the use in marine geological mapping – CAR.G. and P.N.R.A. Projects. In: 27th IAS Meeting of Sedimentologists, Alghero, pp. 85–90. ISBN 978-88-7587-554.

Crosta, X., Romero, O., Armand, L.K., Pichon, J.J., 2005. The biogeography of major diatom taxa in Southern Ocean sediments: 2. Open Ocean related species. Palaeogeogr. Palaeoclimatol. Palaeoecol. 223 (1–2), 66–92.

Crosta, X., Etourneau, J., Orme, L.C., Dalaiden, Q., Campagne, P., Swingedouw, D., Ikehara, M., 2021. Multi-decadal trends in Antarctic Sea-ice extent driven by ENSO–SAM over the last 2,000 years. Nat. Geosci. 14 (3), 156–160.

Cunningham, W.L., Leventer, A., Andrews, J.T., Jennings, A.E., Licht, K.J., 1999. Late Pleistocene-Holocene marine conditions in the Ross Sea, Antarctica: evidence from the diatom record. The Holocene 9 (2), 129–139.

De Castro, S., Hernández-Molina, F.J., Rodríguez-Tovar, F.J., Llave, E., Ng, Z.L., Nishida, N., Mena, A., 2020. Contourites and bottom current reworked sands: Bed facies model and implications. Mar. Geol. 428, 106267.

DeMaster, 1981. The supply and accumulation of silica in the marine environment. Geochim. Cosmochim. Acta 45, 1715–1732.

Di Roberto, A., Colizza, E., Del Carlo, P., Petrelli, M., Finocchiaro, F., Kuhn, G., 2019. First marine cryptotephra in Antarctica found in sediments of the western Ross Sea correlates with englacial tephras and climate records. Sci. Rep. 9 (1), 1–10.

Domack, E.W., Mcclennen, C.E., 1996. Accumulation of glacial marine sediments in fjords of the Antarctic Peninsula and their use as late Holocene paleoenvironmental indicators. Found. Ecol. Res. West Antarc. Peninsula 70, 135–154.

Domack, E.W., Jacobson, E.A., Shipp, S., Anderson, J.B., 1999. Late Pleistocene–Holocene retreat of the West Antarctic Ice-Sheet system in the Ross Sea: Part 2—sedimentologic and stratigraphic signature. Geol. Soc. Am. Bull. 111 (10), 1517–1536.

Domack, E.W., Leventer, A., Root, S., Ring, J., Williams, E., Carlson, D., Burr, G., 2003. Marine sedimentary record of natural environmental variability and recent warming in the Antarctic Peninsula. Antarc. Peninsula Clim. Variab. Hist. Paleoenviron. Perspect. 79, 205–224.

Dunbar, R.B., Leventer, A.R., Stockton, W.L., 1989. Biogenic sedimentation in McMurdo sound, Antarctica. Mar. Geol. 85 (2–4), 155–179.

Erofeeva, S.Y., Padman, L., Egbert, G., 2005. Assimilation of ship-mounted ADCP data for barotropic tides: Application to the Ross Sea. J. Atmos. Oceanic Technol. 22 (6), 721–734.

Escutia, C., Brinkhuis, H., 2014. From greenhouse to icehouse at the Wilkes Land Antarctic margin: IODP Expedition 318 synthesis of results. In: Developments in Marine Geology, Vol. 7. Elsevier, pp. 295–328.

Escutia, C., De Santis, L., Donda, F., Dunbar, R.B., Cooper, A.K., Brancolini, G., Eittreim, S.L., 2005. Cenozoic ice sheet history from East Antarctic Wilkes Land continental margin sediments. Glob. Planet. Chang. 45 (1–3), 51–81.

Finocchiaro, F., Langone, L., Colizza, E., Fontolan, G., Giglio, F., Tuzzi, E., 2005. Record of the early Holocene warming in a laminated sediment core from Cape Hallett Bay (Northern Victoria Land, Antarctica). Glob. Planet. Chang. 45 (1–3), 193–206.

Friedman, G.M., Sanders, J.E., 1978. Principles of Sedimentology. Wiley.

Golledge, N.R., Clark, P.U., He, F., Dutton, A., Turney, C.S.M., Fogwill, C.J., Carlson, A. E., 2021. Retreat of the Antarctic Ice Sheet during the Last Interglaciation and implications for future change. Geophys. Res. Lett. 48 (17) e2021GL094513.

Griffith, T.W., Anderson, J.B., 1989. Climatic control of sedimentation in bays and fjords of the northern Antarctic Peninsula. Mar. Geol. 85 (2–4), 181–204.

Gutowski, M., Breitzke, M., Spieß, V., 2002a. Fast static correction methods for high-frequency multichannel marine seismic reflection data: a high-resolution seismic study of channel-levee systems on the Bengal Fan. Mar. Geophys. Res. 23 (1), 57–75.

Gutowski, M., Bull, J., Henstock, T., et al., 2002b. Chirp sub-bottom profiler source signature design and field testing. Mar. Geophys. Res. 23, 481–492. https://doi.org/10.1023/B:MARI.0000018247.57117.0e.

Halberstadt, A.R.W., Simkins, L.M., Greenwood, S.L., Anderson, J.B., 2016. Past ice-sheet behaviour: retreat scenarios and changing controls in the Ross Sea, Antarctica. Cryosphere 10 (3), 1003–1020.

Hall, B.L., Denton, G.H., 1999. New relative sea-level curves for the southern Scott Coast, Antarctica: evidence for Holocene deglaciation of the western Ross Sea. J. Quat. Sci. 14 (7), 641–650.

Hall, B.L., Denton, G.H., Stone, J.O., Conway, H., 2013. History of the grounded ice sheet in the Ross Sea sector of Antarctica during the Last Glacial Maximum and the last termination. Geol. Soc. Lond. Spec. Publ. 381 (1), 167–181.

Hamilton, E.L., 1979. Sound velocity gradients in marine sediments. J. Acoust. Soc. Am. 65 (4), 909–922.

Hawley, R.L., Waddington, E.D., Alley, R.B., Taylor, K.C., 2003. Annual layers in polar firn detected by borehole optical stratigraphy. Geophys. Res. Lett. 30 (15).

Hodell, D.A., Charles, C.D., Sierro, F.J., 2001. Late Pleistocene evolution of the ocean's carbonate system. Earth Planet. Sci. Lett. 192 (2), 109–124.

Hodgson, D.A., Graham, A.G., Roberts, S.J., Bentley, M.J., Cofaigh, C.Ó., Verleyen, E., Smith, J.A., 2014. Terrestrial and submarine evidence for the extent and timing of the Last Glacial Maximum and the onset of deglaciation on the maritime-Antarctic and sub-Antarctic islands. Quat. Sci. Rev. 100, 137–158.

Jouzel, J., Vaikmae, R., Petit, J.R., Martin, M., Duclos, Y., Stievenard, M., Kotlyakov, V. M., 1995. The two-step shape and timing of the last deglaciation in Antarctica. Clim. Dyn. 11, 151–161.

Khim, B.K., Colizza, E., Lee, J.I., Giglio, F., Ha, S., Bak, Y.S., 2021. Biological productivity and glaciomarine sedimentation in the Central Basin of the northwestern Ross Sea since the last glacial maximum. Polar Sci. 28, 100682.

Leventer, A., Dunbar, R.B., DeMaster, D.J., 1993. Diatom evidence for late Holocene climatic events in Granite Harbor, Antarctica. Paleoceanography 8 (3), 373–386.

Leventer, A., Domack, E., Barkoukis, A., McAndrews, B., Murray, J., 2002. Laminations from the Palmer Deep: a diatom-based interpretation. Paleoceanography 17 (3), PAL-3.

Lobo, F.J., López-Quirós, A., Hernández-Molina, F.J., Pérez, L.F., García, M., Evangelinos, D., Maldonado, A., 2021. Recent morpho-sedimentary processes in Dove Basin, southern Scotia Sea, Antarctica: a basin-scale case of interaction between bottom currents and mass movements. Mar. Geol. 441, 106598.

Lowry, D.P., Golledge, N.R., Bertler, N.A., Jones, R.S., McKay, R., Stutz, J., 2020. Geologic controls on ice sheet sensitivity to deglacial climate forcing in the Ross Embayment, Antarctica. Q. Sci. Adv. 1, 100002.

Lucchi, R.G., Rebesco, M., 2007. Glacial contourites on the Antarctic Peninsula margin: insight for palaeoenvironmental and palaeoclimatic conditions. Geol. Soc. Lond. Spec. Publ. 276 (1), 111–127.

Lucchi, R.G., Camerlenghi, A., Rebesco, M., Colmenero-Hidalgo, E., Sierro, F.J., Sagnotti, L., Caburlotto, A., 2013. Postglacial sedimentary processes on the Storfjorden and Kveithola trough mouth fans: significance of extreme glacimarine sedimentation. Glob. Planet. Chang. 111, 309–326.

McGlannan, A.J., Bart, P.J., Chow, J.M., DeCesare, M., 2017. On the influence of post-LGM ice shelf loss and grounding zone sedimentation on West Antarctic ice sheet stability. Mar. Geol. 392, 151–169.

McMinn, A., Heijnisj, H., Harle, K., McOrist, G., 2001. Late-Holocene climatic change recorded in sediment cores from Ellis Fjord, eastern Antarctica. The Holocene 11 (3), 291–300.

Mezgec, K., Stenni, B., Crosta, X., Masson-Delmotte, V., Baroni, C., Braida, M., Frezzotti, M., 2017. Holocene Sea ice variability driven by wind and polynya efficiency in the Ross Sea. Nat. Commun. 8 (1), 1–12.

Miramontes, E., Cattaneo, A., Jouet, G., Thereau, E., Thomas, Y., Rovere, M., Trincardi, F., 2016. The Pianosa contourite depositional system (northern Tyrrhenian Sea): drift morphology and Plio-Quaternary stratigraphic evolution. Mar. Geol. 378, 20–42.

Miramontes, E., Garreau, P., Caillaud, M., Jouet, G., Pellen, R., Hernández-Molina, F.J., Cattaneo, A., 2019. Contourite distribution and bottom currents in the NW Mediterranean Sea: Coupling seafloor geomorphology and hydrodynamic modelling. Geomorphology 333, 43–60.

Morelli, D., Colizza, E., Corradi, N., Finocchiaro, F., Giglio, F., Langone, L., Ridente, D., 2008. Morpho-stratigraphic features in the Edinsto Inlet, a high sedimentation rate in western Ross Sea (Antarctica). In: 5th EGU General AssemblyGeophysical, Research Abstracts, Vol. 10.

Mosola, A.B., Anderson, J.B., 2006. Expansion and rapid retreat of the West Antarctic Ice Sheet in eastern Ross Sea: possible consequence of over-extended ice streams? Quat. Sci. Rev. 25 (17–18), 2177–2196.

Mugford, R.I., Dowdeswell, J.A., 2011. Modeling glacial meltwater plume dynamics and sedimentation in high-latitude fjords. J. Geophys. Res. Earth 116 (F1).

Narcisi, B., Petit, J.R., 2021. Englacial Tephras of East Antarctica.

Neder, C., Fofonova, V., Androsov, A., Kuznetsov, I., Abele, D., Falk, U., Jerosch, K., 2022. Modelling suspended particulate matter dynamics at an Antarctic fjord impacted by glacier melt. J. Mar. Syst. 231, 103734.

Nielsen, S.H., Koç, N., Crosta, X., 2004. Holocene climate in the Atlantic sector of the Southern Ocean: controlled by insolation or oceanic circulation? Geology 32 (4), 317–320.

Pahnke, K., Sachs, J.P., 2006. Sea surface temperatures of southern midlatitudes 0–160 kyr BP. Paleoceanography 21 (2).

Presti, M., De Santis, L., Brancolini, G., Harris, P.T., 2005. Continental shelf record of the East Antarctic Ice Sheet evolution: seismo-stratigraphic evidence from the George V Basin. Quat. Sci. Rev. 24 (10–11), 1223–1241.

Prothro, L.O., Majewski, W., Yokoyama, Y., Simkins, L.M., Anderson, J.B., Yamane, M., Ohkouchi, N., 2020. Timing and pathways of East Antarctic ice sheet retreat. Quat. Sci. Rev. 230, 106166.

Quinn, R., Bull, J.M., Dix, J.K., 1997. Imaging wooden artefacts using Chirp sources. Archaeol. Prospect. 4 (1), 25–35.

Rebesco, M., Camerlenghi, A., De Santis, L., Domack, E., Kirby, M., 1998. Seismic stratigraphy of Palmer Deep: a fault-bounded late Quaternary sediment trap on the inner continental shelf, Antarctic Peninsula Pacific margin. Mar. Geol. 151 (1–4), 89–110.

Rebesco, M., Domack, E., Zgur, F., Lavoie, C., Leventer, A., Brachfeld, S., Willmott, V., Halverson, G., Truffer, M., Scambos, T., Smith, J., Pettit, E., 2014a. Boundary condition of grounding lines prior to collapse, Larsen-B Ice Shelf. Antarct. Sci. 345 (6202), 1354–1358.

Rebesco, M., Hernández-Molina, F.J., Van Rooij, D., Wåhlin, A., 2014b. Contourites and associated sediments controlled by deep-water circulation processes: state-of-the-art and future considerations. Mar. Geol. 352, 111–154.

Rebesco, M., Özmaral, A., Urgeles, R., Accettella, D., Lucchi, R.G., Rüther, D., Winsborrow, M., Llopart, J., Caburlotto, A., Lantzsch, H., Hanebuth, T.J.J., 2016. Evolution of a high-latitude sediment drift inside a glacially-carved trough based on high-resolution seismic stratigraphy (Kveithola, NW Barents Sea). Quat. Sci. Rev. 147, 178–193.

Reimer, P.J., Bard, E., Bayliss, A., Beck, J.W., Blackwell, P.G., Ramsey, C.B., Van Der Plicht, J., 2013. IntCal13 and Marine13 radiocarbon age calibration curves 0–50,000 years cal BP. Radiocarbon 55 (4), 1869–1887.

Shevenell, A.E., Ingalls, A.E., Domack, E.W., Kelly, C., 2011. Holocene Southern Ocean surface temperature variability west of the Antarctic Peninsula. Nature 470 (7333), 250–254.

Ship, S., Anderson, J., Domack, E., 1999. Late Pleistocene–Holocene retreat of the West Antarctic Ice-Sheet system in the Ross Sea: part 1—geophysical results. Geol. Soc. Am. Bull. 111 (10), 1486–1516.

Shipp, S.S., Wellner, J.S., Anderson, J.B., 2002. Retreat signature of a polar ice stream: sub-glacial geomorphic features and sediments from the Ross Sea, Antarctica. Geol. Soc. Lond. Spec. Publ. 203 (1), 277–304.

Simkins, L.M., Greenwood, S.L., Anderson, J.B., 2018. Diagnosing ice sheet grounding line stability from landform morphology. Cryosphere 12 (8), 2707–2726.

Sjunneskog, C., Taylor, F., 2002. Postglacial marine diatom record of the Palmer deep, Antarctic Peninsula (ODP Leg 178, Site 1098) 1. Total diatom abundance. Paleoceanography 17 (3), PAL-4.

Slabon, P., Dorschel, B., Jokat, W., Myklebust, R., Hebbeln, D., Gebhardt, C., 2016. Greenland ice sheet retreat history in the northeast Baffin Bay based on high-resolution bathymetry. Quat. Sci. Rev. 154, 182–198.

Small, R.J., 1983. Lateral moraines of glacier de Tsidjiore Nouve: form, development, and implications. J. Glaciol. 29 (102), 250–259.

Smith, J.A., Graham, A.G., Post, A.L., Hillenbrand, C.D., Bart, P.J., Powell, R.D., 2019. The marine geological imprint of Antarctic ice shelves. Nat. Commun. 10 (1), 1–16.

Still, H., Campbell, A., Hulbe, C., 2019. Mechanical analysis of pinning points in the Ross Ice Shelf, Antarctica. Ann. Glaciol. 60 (78), 32–41.

Stokes, C.R., Clark, C.D., 2001. Palaeo-ice streams. Quaternary Science Reviews 20 (13), 1437–1457.

Stow, D., Smillie, Z., 2020. Distinguishing between deep-water sediment facies: turbidites, contourites and hemipelagites. Geosciences 10 (2), 68.

Tesi, T., Belt, S.T., Gariboldi, K., Muschitiello, F., Smik, L., Finocchiaro, F., Langone, L., 2020. Resolving Sea ice dynamics in the North-Western Ross Sea during the last 2.6 ka: from seasonal to millennial timescales. Quat. Sci. Rev. 237, 106299.

Van Beek, P., Reyss, J.L., Paterne, M., Gersonde, R., van Der Loeff, M.R., Kuhn, G., 2002. 226Ra in barite: absolute dating of Holocene Southern Ocean sediments and reconstruction of sea-surface reservoir ages. Geology 30 (8), 731–734.

Weber, M.E., Clark, P.U., Kuhn, G., Timmermann, A., Sprenk, D., Gladstone, R., Ohlwein, C., 2014. Millennial-scale variability in Antarctic ice-sheet discharge during the last deglaciation. Nature 510 (7503), 134–138.

Wellner, J.S., Lowe, A.L., Shipp, S.S., Anderson, J.B., 2001. Distribution of glacial geomorphic features on the Antarctic continental shelf and correlation with substrate: implications for ice behavior. J. Glaciol. 47 (158), 397–411.

Willmott, V., Domack, E., Padman, L., Canals, M., 2007. Glaciomarine sediment drifts from Gerlache Strait, Antarctic Peninsula. Glacial Sediment. Proc. Prod. 67–84.